nature aging

Article

https://doi.org/10.1038/s43587-025-00961-8

Elastin-derived extracellular matrix fragments drive aging through innate immune activation

Received: 19 July 2024

Accepted: 13 August 2025

Published online: 29 September 2025

Check for updates

Junzhi Yi[1,2,7], Yixuan Wang[1,2,7], Hairu Sui[1,2,7], Zhichu Chen[1,2,7], Tianning Ye[1,2], Yuliang Zhong[1,2], Jingyi Qian[1,2], Bingbing Wu[3], Jiayun Huang[1,2], Tian Tian[1,2], Fangyuan Bao[1,2], Xuri Chen[1,2], Xiao Xiao[1,2], Jiasheng Wang[1,2], Jiajie Hu[1,2], Yujuan Xie[1,2], Hui Zhang[1,2], Pan Jin[3], Xiaoping Xia[3], Xudong Yao[3], Yishan Chen[4], Zi Yin[2,5], Weiliang Shen[1,2,5], Jing Zhou[1,2,5], Xiaohui Zou[6], Hua Liu[1,2,4,5] & Hongwei Ouyang[1,2,4,5] ✉

The roles of cells in systemic aging have been systematically investigated, while the roles of the extracellular matrix (ECM) and its degradation have been largely overlooked. Herein, we show that the serum contents of elastin-, hyaluronic acid- and fibronectin-derived fragments are all positively correlated with age. Elastin-derived fragments exhibited the most potent lifespan-shortening effects in mice and a positive correlation with various aging indicators in a human cohort (n = 1,068). Mechanistically, the VGVAPG oligopeptide (E-motif) in elastin-derived fragments activated monocytes and macrophages through NEU1, a component of the elastin receptor complex, which consequently caused an inflammatory response. Therapeutically, a NEU1 inhibitor extended lifespan by up to 17% in wild-type naturally aged mice and alleviated aging-related phenotypes in wild-type mice, immune-humanized mice and pigs. This study uncovers that degraded ECM acts as a circulating driver of aging, providing an anti-aging intervention strategy focused on particular elastin fragment signals.

Human tissues are composed of cells and extracellular matrix (ECM), both of which undergo degenerative changes during aging[1]. While current research on aging primarily focuses on cellular aging and associated events, such as cell senescence, stem cell exhaustion, genomic instability, telomere attrition and epigenetic alterations[2], ECM alterations and their impacts during aging remain underexplored. In instances of tissue damage or degenerative changes, there is abnormal remodeling and excessive degradation of the ECM, leading to an increase in free ECM fragments in urine and bodily fluids, including serum and synovial fluid. Aging-associated diseases, such as atherosclerosis[3,4] and chronic obstructive pulmonary disease (COPD)[5], are associated with elevated levels of elastin (ELN) fragments in serum. Similarly, cartilage degeneration causes the release of various types of collagen (COL) fragments and fibronectin (FN) fragments into the synovial fluid and/or serum[6,7]. Breast cancer and bladder cancer increase the levels of hyaluronic acid (HA) fragments in serum and the tumor microenvironment,

[1]Department of Sports Medicine of the Second Affiliated Hospital and Liangzhu Laboratory, Zhejiang University School of Medicine, Hangzhou, China. [2]Dr. Li Dak Sum & Yip Yio Chin Center for Stem Cells and Regenerative Medicine, Zhejiang University School of Medicine, Hangzhou, China. [3]The Fourth Affiliated Hospital of School of Medicine and International School of Medicine, International Institutes of Medicine, Zhejiang University, Yiwu, China. [4]Zhejiang University–University of Edinburgh Institute, Zhejiang University School of Medicine, Haining, China. [5]China Orthopedic Regenerative Medicine Group (CORMed), Hangzhou, China. [6]Central Laboratory, The First Affiliated Hospital, Zhejiang University School of Medicine, Hangzhou, China. [7]These authors contributed equally: Junzhi Yi, Yixuan Wang, Hairu Sui, Zhichu Chen. ✉e-mail: hwoy@zju.edu.cn

respectively[8,9]. These findings suggest that free ECM fragments in bodily fluids may correlate with systemic aging.

In recent years, the concept of 'matrikines' has been introduced, referring to ECM fragments that act as cytokines and can exert multiple biological effects, including tissue impairment and/or degeneration[10]. For example, HA fragments released from skin and cancer tissue cause inflammatory bowel disease and cancer-related inflammation and angiogenesis, respectively[9,11]. FN fragments accelerate osteoarthritis and periodontitis[7,12]. In terms of mechanisms, our previous study and other research have found that matrikines can activate the immune system, leading to an inflammatory state and immune dysfunction. We have shown that type II COL fragments released from cartilage into the peripheral blood activate $CD4^+$ T cells, promoting their differentiation into T helper 17 (T_H17) cells and the secretion of interleukin-17 (IL-17), which results in liver damage[13]. ELN fragments activate T cells to secrete IL-17 and stimulate oxidative stress and monocyte migration, contributing to the progression of COPD and atherosclerosis, respectively[14,15]. Therefore, abnormal immune activation and the secretion of inflammatory factors are important mechanisms by which matrikines lead to tissue impairment. However, the long-term effects of matrikines on systemic tissue alterations and the corresponding mechanisms remain unclear.

Immune degeneration and chronic inflammation have been widely related to aging. Age-related dysfunction of immune cells has been reported to cause skeletal aging[16], brown adipose tissue aging[17] and age-related changes in gut microbiota[18]. Specific induction of aging in the entire immune system or only T cells causes systemic chronic inflammation and aging of solid organs[19,20]. Chronic inflammation is generally accompanied by, and forms a positive feedback loop with, immune degeneration[19–21]. The reasons for age-related dysfunction of the immune system and inflammation are complex, with previous studies attributing these conditions mainly to the senescence-associated secretory phenotype and gut microbiota[18,22]. Although matrikines have been reported to cause immune activation and inflammation in certain diseases, it remains unknown whether long-term upregulation of matrikines contributes to age-related immune dysfunction and chronic inflammation. Therefore, we hypothesized that an age-related increase in particular matrikines induces systemic aging through immune dysfunction, representing a new target for anti-aging interventions.

Results

ECM fragments (matrikines) are differentially associated with aging

To comprehensively explore the relationship between matrikines and aging at a systemic level, we quantified the serum levels of ELN, HA, FN and COL fragments, the major ECM components in the body[23], in humans and mice across different ages. Linear regression analysis indicated a significantly positive correlation between the concentrations of all these matrikines and age in both species (Fig. 1a,b). To assess causality, we administered these fragments by tail vein injection in mice (Fig. 1c). Survival curve analysis demonstrated a reduction in lifespan in the ELN, HA and FN groups compared to the vehicle group, with ELN fragments showing the most substantial effect (Fig. 1d).

For healthspan examination (Fig. 1c), all treated mice showed a gradual increase in body weight compared to the vehicle group, with ELN fragments exerting the most pronounced effect (Fig. 1e). Moreover, the ratio of fat tissue to body weight was markedly increased in the ELN group and slightly increased in the HA group at the endpoint of the experiments (36 weeks of age) (Fig. 1f). The ratio of lean tissue to body weight was significantly decreased in the ELN and FN groups, while it was slightly decreased in the HA and COL groups (Fig. 1f). These results indicate that long-term treatment with ELN fragments promotes obesity. Running and hanging tests showed that ELN fragments and, to a lesser degree, HA fragments reduced the sport ability and muscle strength of mice (Fig. 1g and Supplementary Fig. 1a). Blood biochemistry analysis revealed significant impairment of liver function in the ELN group and moderate impairment in the HA and FN groups, as evidenced by the levels of aspartate aminotransferase (AST) and alanine aminotransferase (ALT) in serum (Fig. 1h). All inflammatory markers, including IL-1, tumor necrosis factor (TNF) and IL-6, were upregulated in the ELN group, indicating systemic chronic inflammation (Fig. 1i and Supplementary Fig. 1b). Upregulation of some of these inflammatory markers was also observed in the HA and FN groups (Fig. 1i and Supplementary Fig. 1b). Furthermore, qPCR analysis of aging- and inflammation-related genes, including *P16^{INK4A}*, *P21*, *P53*, *Il1b*, *Il6* and *Tnf*, across various organs (liver, heart, kidney, spleen, white adipose tissue (WAT), muscle and lung) revealed that most of the genes in these tissues were upregulated in the ELN group but not in the other groups (Fig. 1j).

Collectively, these findings suggest that circulating matrikine levels increase with age. ELN fragments, at the physiological concentration that mimics the aging process (Supplementary Fig. 2), appear to be the most potent accelerators of aging, while HA and FN fragments promote aging to a lesser degree.

ELN fragments and their VGVAPG oligopeptide (E-motif) reduce healthspan and lifespan

To validate the pro-aging effects of endogenous ELN fragments, we collected serum-derived ELN fragments from old mice (age 20 months; ECO) or young mice (age 12 weeks; ECY) and injected them into young recipient mice (Extended Data Fig. 1a). ECO, but not ECY, significantly increased body weight (Extended Data Fig. 1b) and impaired the fat and lean tissue percentages (Extended Data Fig. 1c) compared to the vehicle group. ECO also upregulated serological markers of hepatic impairment (AST and ALT; Extended Data Fig. 1d,e) and systemic inflammation (IL-1 and MCP-1; Extended Data Fig. 1g) and reduced locomotor

Fig. 1 | Matrikines are differentially associated with aging. a, Correlation between the serum levels of different matrikines (ELN, HA, FN and COL fragments; measured by ELISA) and age in humans of varying ages. The red dashed line represents the linear regression line ($n = 100$ per group; $P < 0.0001$ for each group). **b**, Positive correlation between the serum levels of different matrikines (ELN, HA, FN and COL fragments; measured by ELISA) and age in mice across five different age points (3, 9, 15, 21 and 27 months). The red dashed line represents the linear regression line (ELN, COL: $n = 32$, HA, FN: $n = 31$; $P < 0.0001$ for each group). **c**, Schematic diagram illustrating the experimental design of injecting matrikines into mice through the tail vein to study their effects on healthspan and lifespan. w, weeks; Kill, time point of animal killing. Illustration was created using FigDraw. **d**, Survival curves of mice injected with vehicle or matrikines ($n = 4$ per group; ELN versus vehicle $P = 0.0266$ by log-rank test and $P = 0.0328$ by Gehan–Breslow–Wilcoxon test). **e**, Body weight changes in mice injected with vehicle (PBS) or matrikines ($n = 4$ per group over time; ELN versus vehicle: at 28 weeks $P = 0.0105$, at 32 weeks $P = 0.0011$, at 36 weeks $P = 0.0003$). **f**, Percentage of fat tissue and lean tissue relative to body weight in mice treated with vehicle or ELN, HA, FN and COL fragments twice a week for 24 weeks ($n = 4$ per group; fat tissue: ELN versus vehicle $P = 0.0170$; lean tissue: ELN versus vehicle $P = 0.0198$, FN versus vehicle $P = 0.0469$). **g**, Schematic representation of the treadmill test (left) and analysis of the number of electric shocks administered (right) ($n = 4$ per group; ELN versus vehicle $P = 0.0291$, HA versus vehicle $P = 0.0247$). **h**, Serum levels of the hepatic markers AST and ALT ($n = 4$ per group; AST: ELN versus vehicle $P = 0.0329$, HA versus vehicle $P = 0.0451$; ALT: ELN versus vehicle $P = 0.0076$). **i**, Serum levels of the inflammatory cytokines IL-1 and TNF ($n = 4$ per group; IL-1: ELN versus vehicle $P = 0.0130$; TNF: ELN versus vehicle $P = 0.0017$, HA versus vehicle $P = 0.0129$). **j**, qPCR analysis showing the expression of *P16^{INK4A}*, *P21*, *P53*, *Il1b*, *Il6* and *Tnf* in various organs (liver, heart, kidney, spleen, WAT, muscle and lung) of mice. The heatmap illustrates the fold changes relative to the mean values of the vehicle group ($n = 4$ per group). $^*P < 0.05$, $^{**}P < 0.01$, $^{***}P < 0.001$ compared to the vehicle group. Statistical tests: Pearson correlation coefficients with a two-tailed 95% confidence interval (**a**, **b**); log-rank test and Gehan–Breslow–Wilcoxon test (**d**); two-way ANOVA (**e**); unpaired two-tailed Student's *t* test (equal variance) or unpaired two-tailed *t* test with Welch's correction (unequal variance) with a 95% confidence interval (**f**–**j**). Data are presented as mean values ± s.d. (**e**–**i**).

https://doi.org/10.1038/s43587-025-00961-8

activity (Extended Data Fig. 1f). Histological analyses revealed adipocyte hypertrophy in WAT and exacerbated hepatic steatosis compared to the vehicle group (Extended Data Fig. 1h). To further confirm that ELN fragments, not other impurities, induce the above phenomenon, we injected ECO with IgG or an anti-ELN antibody (Extended Data Fig. 1j). The anti-ELN antibody alleviated the ECO-induced aging phenotype (Extended Data Fig. 1k–o). To investigate the reason behind the age-related ELN fragment accumulation, we treated old mice with senolytics (dasatinib and quercetin (D + Q)) (Extended Data Fig. 1p), as cellular senescence is a recognized hallmark of aging[24]. Treatment with D + Q significantly reduced the serum content of ELN fragments in old mice (Extended Data Fig. 1q). Previous studies have identified two main elastases: macrophage elastase (ME; also known as MMP12) and neutrophil elastase (NE)[25]. Neutrophils and macrophages were separated after D + Q treatment. D + Q decreased the expression of *P16*^{INK4A} in both neutrophils and macrophages (Extended Data Fig. 1r). D + Q also decreased the NE and ME contents in the supernatants of separated neutrophils and macrophages, respectively (Extended Data Fig. 1s). Treatment with an NE inhibitor and an ME inhibitor decreased the amount of ELN fragments in old mice (Extended Data Fig. 1t). These results indicate that elastases derived from aged myeloid cells can increase the serum levels of ELN fragments during aging.

After identifying the significant pro-aging effects of ELN fragments, we next sought to determine the specific sequence within ELN that is responsible for these detrimental effects. ELN predominantly comprises two conserved motifs: a glycine (G)–valine (V)-rich motif

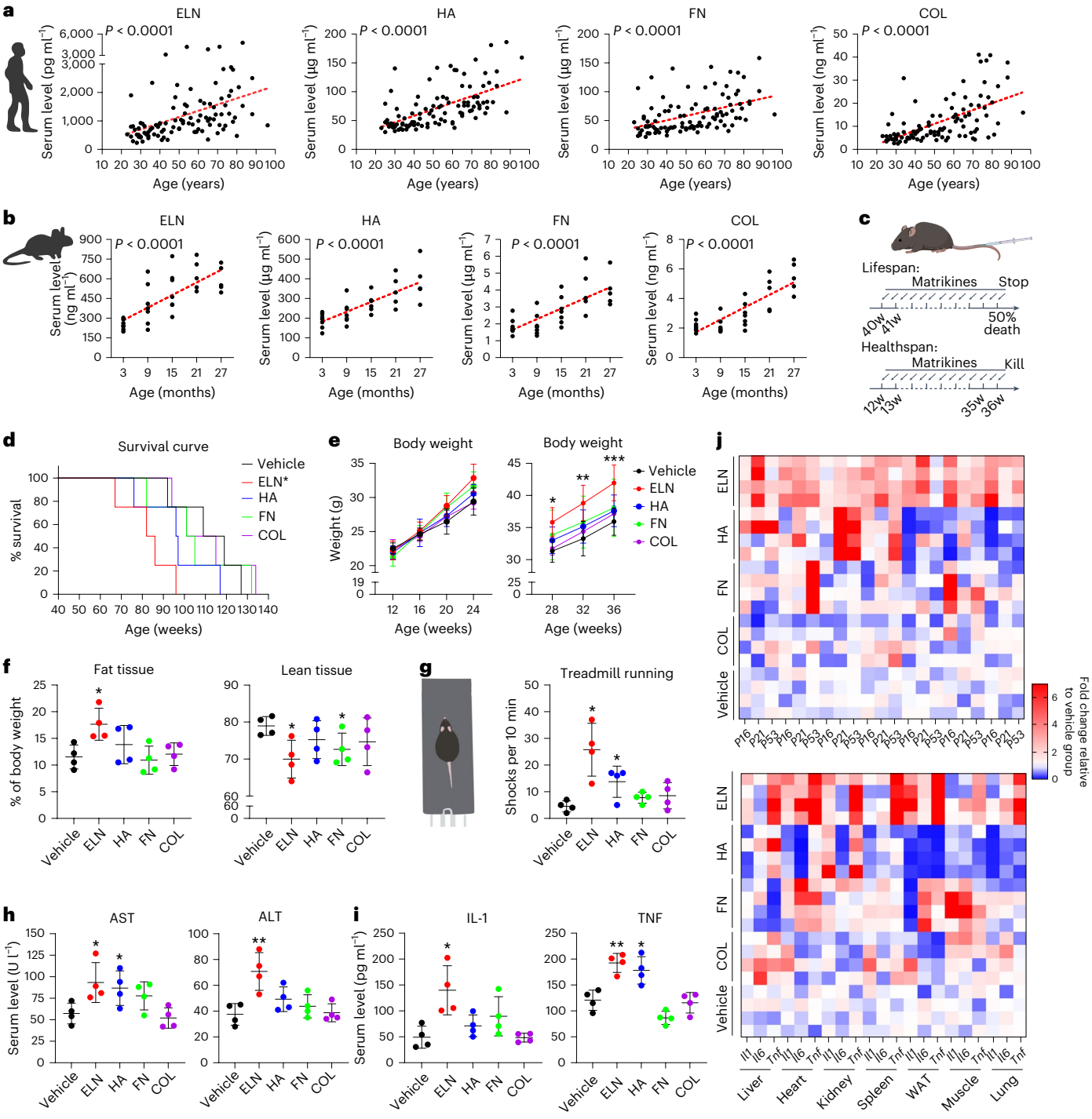

and an alanine (A)–lysine (K)-rich motif (AAH51649.1). To determine their respective roles, we intravenously injected mice with either a VGVAPG-containing motif (referred to as the E-motif) or an A–K-rich motif (poly(A/K)) (Fig. 2a). Remarkably, E-motif treatment significantly decreased lifespan, while poly(A/K) had minimal impact on lifespan compared to the vehicle group (Fig. 2b). Previous studies have reported that a heterotrimeric receptor complex, the ELN receptor complex (ERC), is responsible for the recognition of ELN fragments[26]. ELN-binding protein, positioned on the outermost part of the ERC, serves as the direct binding site only for the GxxPG motif (especially E-motif) but not for poly(A/K)[27,28]. These findings prompted us to further investigate the effects of E-motif on various aspects of healthspan and aging, considering ERC as a mediator of this phenomenon (in this study, ELN fragments generally refer to degraded ELN, while E-motif specifically indicates the VGVAPG-containing sequence).

We then explored the aging-related effects induced by long-term E-motif treatment (Fig. 2a and Supplementary Fig. 3). Mice in the E-motif group exhibited an increase in body weight (Fig. 2c), an increased percentage of fat tissue and greater abdominal fat weight, accompanied by a decreased percentage of lean tissue relative to body weight (Fig. 2d,e and Extended Data Fig. 2a), indicating that E-motif promotes obesity. The animals also exhibited impaired motor ability in the treadmill test and open field assay (Fig. 2f,g), while the latency to fall in the wire hang test was decreased (Extended Data Fig. 2b). qPCR analysis across multiple tissues revealed that the majority of aging- and inflammation-related genes were upregulated in the E-motif group (Supplementary Fig. 4), which corresponded with P16-3MR mice[29] showing a significantly higher P16 signal in the E-motif group (Fig. 2h). X-ray imaging revealed that the kyphosis index was significantly reduced in the E-motif group (Fig. 2i), indicating a hunchback deformity. E-motif treatment also induced significant blood biochemical alterations (Fig. 2j), including elevated levels of AST and ALT (Fig. 2k), which are indicative of liver degeneration. Furthermore, increased levels of triglyceride (TG), low-density lipoprotein (LDL) and glucose (GLU) (Extended Data Fig. 2c) were observed, suggesting metabolic disturbances and obesity. The levels of inflammatory markers, including IL-1, IL-6, MCP-1, TNF and IFNγ, were significantly higher in the E-motif group, indicating a heightened inflammatory state (Fig. 2l and Extended Data Fig. 2d,e), which is a hallmark of aging[30]. Histomorphological analysis revealed several degenerative changes in the E-motif group, including an enlarged area of adipocytes in WAT (Fig. 2m), which corresponds with obesity and metabolic dysfunction[31]; thinner epidermis and looser dermis in the skin (Fig. 2n); a reduced cross-sectional area of muscle fibers (Extended Data Fig. 2f); and increased liver lipid vacuoles and TG content (Fig. 2o). Micro-computed tomography (micro-CT) analysis revealed osteoporosis-related changes in the E-motif group (Extended Data Fig. 2g). To further demonstrate that it is the E-motif rather than an arbitrary oligopeptide that can induce the above phenomenon, we also administered a scrambled oligopeptide of E-motif to the mice. The scrambled oligopeptide failed to induce obesity, changes in fat and lean tissue, reduced locomotor activity, and degeneration of the liver and WAT (Extended Data Fig. 2h–m).

In this section, we present compelling evidence that ELN fragments and the E-motif within ELN are potent inducers of reduced lifespan and unhealthy aging, from the whole body to the molecular level.

E-motif promotes aging partly through adaptive immune activation

To investigate the mechanisms underlying E-motif-induced aging phenotypes, we first performed transcriptomic profiling across multiple organs and tissues 24 h after a single E-motif injection (Extended Data Fig. 3a). Peripheral blood mononuclear cells (PBMCs) exhibited the most pronounced changes according to the number of differentially expressed genes (DEGs) and volcano plot analysis (Extended Data Fig. 3b–d). Further Gene Ontology (GO) analysis and gene set enrichment analysis (GSEA) revealed an upregulation of terms related to immune responses, inflammation, proliferation and metabolic disease in the PBMCs of the E-motif group compared to the control group (Extended Data Fig. 3e,f). To delve deeper into the immunological effects of E-motif, we performed cytometry by time-of-flight (CyTOF) analysis on $CD45^+$ PBMCs from mice that received E-motif injections twice a week for 24 weeks (Fig. 3a). The *t*-distributed stochastic neighbor embedding (*t*-SNE) analysis revealed obvious upregulation of marker expression in $CD4^+$ T cells (CD3E, CD4), $CD8^+$ T cells (CD3E, CD8) and B cells (CD19, B220), as well as an increase in the proportion of the corresponding cell clusters, in the E-motif group compared to the control group (Fig. 3b and Extended Data Fig. 3i). SPADE (spanning-tree progression analysis of density-normalized events) and flow cytometry analyses confirmed the increased proportions of T cells (both $CD4^+$ and $CD8^+$ T cells) and B cells in the E-motif group (Fig. 3c,d and Extended Data Fig. 3j).

To ascertain the specific roles of T and B (T/B) cells in E-motif-induced aging, we used T/B cell-deficient *Rag1*$^{-/-}$ mice (Rag) and Rag mice reconstituted with T/B cells (Rag + T/B) for healthspan and lifespan examinations (Fig. 3e and Extended Data Fig. 4a). E-motif injection significantly shortened lifespan in Rag + T/B mice but not in Rag mice (Fig. 3f). Similarly, E-motif induced weight gain, increased fat mass (including abdominal fat) and reduced lean mass only in Rag + T/B mice compared to the corresponding vehicle control (Fig. 3g,h and Extended Data Fig. 4b). Unlike Rag + T/B mice, Rag mice did not show significant elevations in serological markers of liver function (AST and ALT) and inflammation (MCP-1, IL-1, TNF, IL-6 and IFNγ) between E-motif and vehicle treatments (Fig. 3i–k and Extended Data Fig. 4c). Histological examination (bone, WAT, skin, liver and muscle) and gene expression analysis (*P16*^{INK4A}, *P21*, *P53*, *Il1b*, *Il6* and *Tnf*) of various tissues revealed only slight changes between the E-motif and vehicle groups in Rag mice (Extended Data Fig. 4d–h and Supplementary Fig. 5).

To dissect the changes in T/B cells after 24 weeks of E-motif treatment, we performed single-cell RNA sequencing (RNA-seq) on sorted T/B cells from the spleen, the weight of which was significantly increased in the E-motif group (Extended Data Fig. 5a,b). Uniform manifold approximation and projection (UMAP) analysis showed a clear separation between the T/B cell populations (Extended Data Fig. 5c). DEG analysis demonstrated that T cells, but not B cells, showed remarkable differential gene expression, with an upregulation of proinflammatory genes (*Ccl5*, *Cxcr3*, etc.) in the E-motif group (Extended Data Fig. 5d). Violin plots and UMAP feature plots consistently demonstrated elevated expression of *Cd8a*, *P53*, *Ifng* and *Gzmk* in T cells from the E-motif group (Fig. 3l and Extended Data Fig. 5e). GO analysis of the DEGs in T cells revealed prominent enrichment in pathways related to cell–cell adhesion, leukocyte proliferation and T cell activation (Extended Data Fig. 5f). Further clustering identified multiple T cell subpopulations. E-motif treatment increased the proportions of the $CD4^+IFN\gamma^+$ T_H1, $CD4^+EOMES^+GZMK^+$ cytotoxic T (Tc), $KLRG1^+FOXP3^+$ regulatory T (T_{reg}) and $CD8^+TBX21^+$ type 1 Tc (Tc1) cell subsets while reducing naive T cells (Fig. 3m,n). The genes and subpopulations that were upregulated in the E-motif group are closely related to inflammaging[19,32,33]. GO enriched pathway and DEG analyses indicated that most T cell subpopulations in the E-motif group showed a similar state shift (Extended Data Fig. 5g,h). Specifically, $CD4^+EOMES^+GZMK^+$ Tc cells were enriched in pathways related to the inflammatory response and chemokine-mediated signaling, while $CD4^+IFN\gamma^+$ T_H1 cells showed upregulation of chemotaxis-related programs. $KLRG1^+FOXP3^+$ T_{reg} cells were enriched in pathways related to T cell activation and proliferation (Extended Data Fig. 5g,h).

Collectively, these results demonstrate that abnormal activation of T/B cells, especially a shift in T cells toward a proinflammatory and aging-associated state, has a crucial role in the systemic pro-aging effects of E-motif.

https://doi.org/10.1038/s43587-025-00961-8

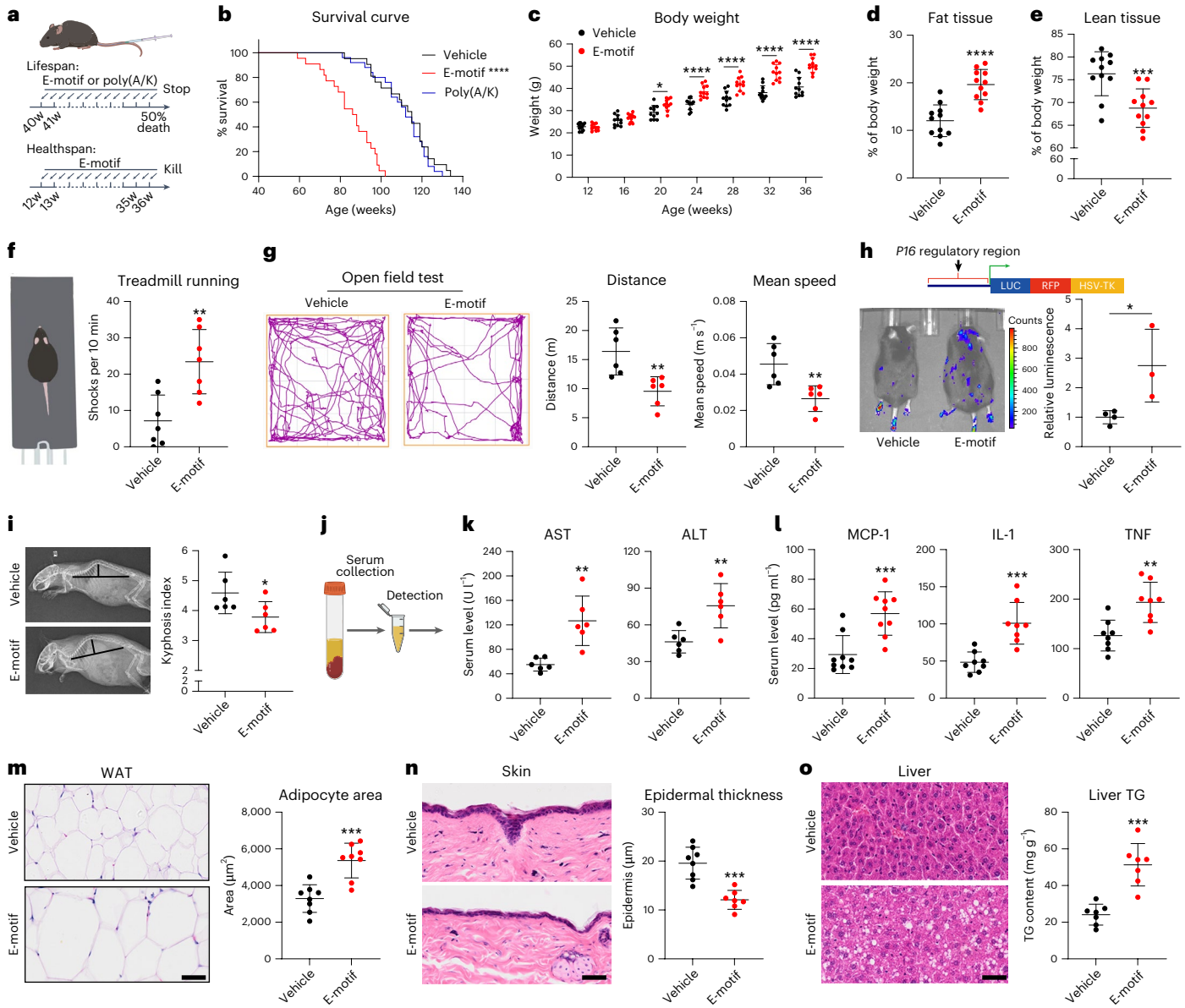

Fig. 2 | E-motif induces an unhealthy and shorter lifespan. a, Schematic diagram illustrating the experimental design of injecting E-motif or poly(A/K) into the tail vein of mice to study their effects on lifespan and healthspan. Illustration was created using FigDraw. **b**, Survival curves of mice injected with vehicle, E-motif or poly(A/K) (vehicle: $n = 21$, E-motif: $n = 22$, poly(A/K): $n = 25$; E-motif versus vehicle: $P < 0.0001$ by log-rank test and $P < 0.0001$ by Gehan–Breslow–Wilcoxon test, poly(A/K) versus vehicle: $P = 0.4473$ by log-rank test and $P = 0.7417$ by Gehan–Breslow–Wilcoxon test). **c**, Body weight changes in mice over time ($n = 11$ per group over time; at 20 weeks $P = 0.0314$, at 24 weeks and after $P < 0.0001$). **d**,**e**, Percentages of fat tissue (**d**) and lean tissue (**e**) relative to body weight at the experimental endpoint ($n = 11$ per group; fat tissue: E-motif versus vehicle $P < 0.0001$, lean tissue: E-motif versus vehicle $P = 0.0009$). **f**, Schematic representation of the treadmill test (left) and analysis of the number of electric shocks administered (right) ($n = 7$ per group; E-motif versus vehicle $P = 0.0025$). **g**, Open field test, including movement trajectories (left), total movement distance (center) and mean speed (right) ($n = 6$ per group; total movement distance: E-motif versus vehicle $P = 0.0054$, mean speed: E-motif versus vehicle $P = 0.0058$). **h**, *P16* gene expression pattern in P16-3MR mice, which carry the luciferase gene expressed under the control of the *P16* regulatory region, allowing spatial visualization of P16-positive senescent cells in vivo through bioluminescence imaging. Left, imaging of mice; right, quantification at the experimental endpoint (vehicle: $n = 4$, E-motif: $n = 3$; E-motif versus vehicle $P = 0.0348$). **i**, Left, representative X-ray images of mice, with black lines indicating how the kyphosis index was measured; right, quantitative analysis of the kyphosis index ($n = 6$ per group; E-motif versus vehicle $P = 0.0450$). **j**, Schematic representation of serum extraction from the peripheral blood of mice. **k**, Blood biochemical tests for AST and ALT levels ($n = 6$ per group; AST: E-motif versus vehicle $P = 0.0065$, ALT: E-motif versus vehicle $P = 0.0076$). **l**, Serum levels of the inflammatory markers MCP-1, IL-1 and TNF (MCP-1: $n = 9$ per group, IL-1 and TNF: $n = 8$ per group; MCP-1: E-motif versus vehicle $P = 0.0006$, IL-1: E-motif versus vehicle $P = 0.0003$, TNF: E-motif versus vehicle $P = 0.0024$). **m**, Representative images of H&E staining of WAT (left) with quantification of the adipocyte area (right) ($n = 8$ per group; E-motif versus vehicle $P = 0.0008$). **n**, Representative images of H&E staining of skin tissue (left) with quantification of epidermal thickness (right) (vehicle: $n = 8$, E-motif: $n = 7$; E-motif versus vehicle $P = 0.0001$). **o**, Representative images of H&E staining of liver tissue (left) with quantification of TG content (right) ($n = 7$ per group; E-motif versus vehicle $P = 0.0001$). $^*P < 0.05$, $^{**}P < 0.01$, $^{***}P < 0.001$, $^{****}P < 0.0001$. Scale bar, 50 μm for **m**, **n** and **o**. Statistical tests: log-rank test and Gehan–Breslow–Wilcoxon test (**b**); two-way ANOVA (**c**); unpaired two-tailed Student's *t* test (equal variance) or unpaired two-tailed *t* test with Welch's correction (unequal variance) with a 95% confidence interval (**d**–**i**, **k**–**o**). Data are presented as mean values ± s.d. (**d**–**i**, **k**–**o**).

https://doi.org/10.1038/s43587-025-00961-8

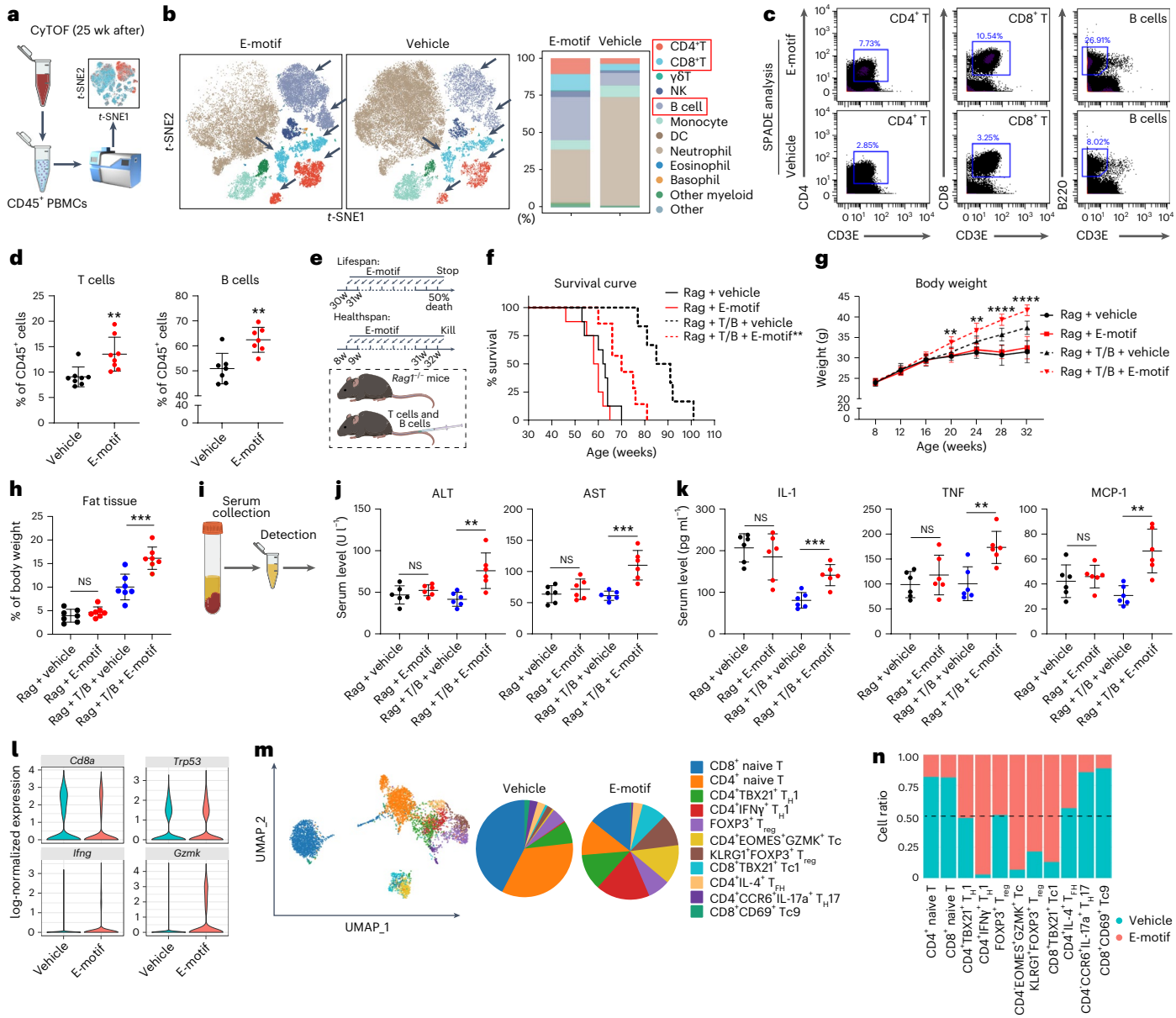

Fig. 3 | E-motif promotes aging partly through adaptive immune activation. **a**, Schematic representation of CyTOF analysis performed after 24 weeks of continuous E-motif treatment. **b**, Left, different cell clusters based on *t*-SNE dimensionality reduction, with arrows indicating clusters with obviously changed proportions; right, quantification of cell proportions, with red boxes indicating obviously changed clusters ($n = 5$ per group). NK, natural killer; DC, dendritic cell. **c**, SPADE analysis and scatter plot illustrating the proportions of cell clusters ($n = 5$ per group). **d**, Flow cytometry validation of the T/B cell proportions (T cells: $n = 8$, B cells: $n = 7$; T cells: E-motif versus vehicle $P = 0.0056$, B cells: E-motif versus vehicle $P = 0.0022$). **e**, Illustrative representation of the tail vein injection of E-motif in Rag or Rag + T/B mice for healthspan and lifespan examinations. **f**, Survival curves of Rag and Rag + T/B mice treated with or without E-motif (Rag + vehicle: $n = 8$, Rag + E-motif: $n = 8$, Rag + T/B + vehicle: $n = 6$, Rag + T/B + E-motif: $n = 7$; Rag + T/B + E-motif versus Rag + T/B + vehicle: $P = 0.0021$ by log-rank test and $P = 0.0032$ by Gehan–Breslow–Wilcoxon test, Rag + E-motif versus Rag + vehicle: $P = 0.2437$ by log-rank test and $P = 0.2671$ by Gehan–Breslow–Wilcoxon test). **g**, Body weight changes in mice over time ($n = 6$ per group over time; Rag + T/B + E-motif versus Rag + T/B + vehicle: at 20 weeks $P = 0.0074$, at 24 weeks $P = 0.0016$, at 28 weeks and after $P < 0.0001$). **h**, Proportion of fat tissue relative to body weight in mice at the experimental endpoint (age 32 weeks) ($n = 7$ per group; Rag + T/B + E-motif versus Rag + T/B + vehicle $P = 0.0008$, Rag + E-motif versus Rag + vehicle $P = 0.2992$). **i**, Schematic representation of serum extraction from the peripheral blood of mice. **j**,**k**, Serum concentrations of markers of liver function (AST and ALT) (**j**) and inflammatory factors (IL-1, TNF and MCP-1) (**k**) ($n = 6$ per group; ALT: Rag + T/B + E-motif versus Rag + T/B + vehicle $P = 0.0044$, Rag + E-motif versus Rag + vehicle $P = 0.3191$; AST: Rag + T/B + E-motif versus Rag + T/B + vehicle $P = 0.0007$, Rag + E-motif versus Rag + vehicle $P = 0.3888$; IL-1: Rag + T/B + E-motif versus Rag + T/B + vehicle $P = 0.0008$, Rag + E-motif versus Rag + vehicle $P = 0.4325$; TNF: Rag + T/B + E-motif versus Rag + T/B + vehicle $P = 0.0034$, Rag + E-motif versus Rag + vehicle $P = 0.3478$; MCP-1: Rag + T/B + E-motif versus Rag + T/B + vehicle $P = 0.0011$, Rag + E-motif versus Rag + vehicle $P = 0.5740$). **l**, Violin plots demonstrating elevated expression of inflammaging-related genes (*Cd8a*, *Trp53*, *Ifng* and *Gzmk*) in the E-motif group ($n = 6$ per group). **m**, UMAP plot showing the clustering and distribution of all T cell subsets after vehicle or E-motif treatment for 24 weeks (left), with pie charts displaying the proportions of T cell subsets in the vehicle and E-motif groups (right) ($n = 6$ per group). T_{FH}, T follicular helper. **n**, Bar plot of the relative abundance of T cell subsets between the vehicle and E-motif groups ($n = 6$ per group). NS, no significance; $^{**}P < 0.01$, $^{***}P < 0.001$, $^{****}P < 0.0001$. Statistical tests: log-rank test and Gehan–Breslow–Wilcoxon test (**f**); two-way ANOVA (**g**); unpaired two-tailed Student's *t* test (equal variance) or unpaired two-tailed *t* test with Welch's correction (unequal variance) with a 95% confidence interval (**d**, **h**, **j**–**k**). Data are presented as mean values ± s.d. (**d**, **g**–**h**, **j**–**k**). Illustrations in panels **a** and **e** were created using FigDraw.

Monocytes and macrophages partly mediate the activation of adaptive immunity by E-motif in a NEU1-dependent manner

To further confirm E-motif-induced inflammaging, we focused on inflammatory factors and detected 22 inflammatory factors after the injection of a dose of E-motif. The time point chosen was 5 weeks after continuous E-motif treatment because lymphocytes began to be upregulated at this time (Supplementary Fig. 6). Among the 22 factors, IL-1β, IL-6, RANTES and MIP-1α showed consistent or obvious upregulation (Supplementary Fig. 7a). As the upregulation of T/B cells has been confirmed, we first investigated whether blocking one factor or several factors could alleviate the upregulation of lymphocytes. Interestingly, blocking two factors mildly prevented the elevation of lymphocytes (Supplementary Fig. 7b), while the synergistic blockade of IL-1β, IL-6 and MIP-1α remarkably alleviated this elevation (Supplementary Fig. 7c). Therefore, we explored whether the synergistic blockade of these three factors using antibodies could alleviate E-motif-induced aging phenotypes. The E-motif + anti group showed significant restoration of obesity (Supplementary Fig. 7d–f), as well as reduced locomotor activity and morphological degeneration of the liver and WAT (Supplementary Fig. 7g–k).

The adaptive immune system, primarily consisting of T/B cells, and inflammaging are often initiated by innate immune activation. At 24 h after a single E-motif treatment, GSEA of PBMC transcriptomic data revealed enrichment of neutrophil chemotaxis and Toll-like receptor (TLR) pathways, indicating activation of innate immunity[34] (Extended Data Fig. 3h), as well as increased chemotaxis or activation of myeloid cells in several solid organs (Extended Data Fig. 3g). To further characterize the myeloid cell clusters affected by E-motif at this time point, we performed CyTOF on $CD45^+$ PBMCs. *t*-SNE analysis and histograms revealed obvious upregulation of marker expression in monocytes and neutrophils, including CD11B, LY6C and LY6G, as well as increased proportions of the corresponding cell clusters (Fig. 4a and Extended Data Fig. 6a). SPADE and flow cytometry analyses confirmed the increased proportions of monocytes and neutrophils (Fig. 4b,c and Extended Data Fig. 6b). To determine which myeloid subset drives the expansion of T/B cells, we transferred neutrophils or monocytes and macrophages (monocytes/macrophages) from E-motif-treated mice into untreated recipient mice (Fig. 4d). Interestingly, only the transfer of monocytes/macrophages induced a significant increase in T/B cells (Fig. 4e). Injection of ECO (ELN fragments collected from old mice) or transfer of monocytes/macrophages from ECO-treated mice also increased the proportion of lymphocytes (Extended Data Fig. 1i). Furthermore, depletion of monocytes/macrophages (Supplementary Fig. 8) in chimeric LysM/iDTR mice abrogated the increase in T/B cells (Fig. 4f,g). Therefore, monocytes/macrophages have a crucial role in mediating the E-motif-induced changes in T/B cells. Interestingly, at this time point (5 weeks of E-motif treatment), no degenerative changes were observed in the liver and WAT, indicating that immune activation preceded tissue degeneration (Supplementary Fig. 9).

To identify the molecular target in monocytes/macrophages that is responsible for mediating the effects of E-motif, we performed transcriptomic sequencing on monocytes/macrophages isolated from mice treated with E-motif or vehicle (Extended Data Fig. 7a,b). GO analysis demonstrated that upregulated genes were mainly enriched in processes related to immune activation and inflammation (Extended Data Fig. 7c). GSEA revealed activation of innate immunity, as well as antigen processing and presentation processes (Extended Data Fig. 7d), further supporting the role of monocytes/macrophages in mediating E-motif-induced aging. GSEA also revealed the upregulation of TLR-related pathways (Extended Data Fig. 7e), inflammatory factor-related processes (Extended Data Fig. 7f) and proliferation-related processes (Extended Data Fig. 7g). As a core component of the ERC, neuraminidase 1 (NEU1) has shown potential as a therapeutic target for local tissue dysfunction[35,36]. NEU1 does not bind the E-motif directly; rather, it acts as a transmembrane signal transducer within the ERC[26], leading to inflammatory states in monocytes/macrophages[37] and upregulating TLR and nuclear factor-κB pathways[38,39], consistent with our GSEA findings. Examination of *Neu1* expression in the transcriptome sequencing data of monocytes/macrophages revealed a significant upregulation in the E-motif group compared to controls, which was confirmed at the protein level by western blot analysis (Fig. 4h,i and Extended Data Fig. 7h).

In vitro, knockdown of *Neu1* blocked the upregulation of IL-1 and IL-6 induced by E-motif in mouse macrophages (Extended Data Fig. 7i,j). We also confirmed the roles of other membrane receptors enriched in RNA-seq data and found that the double knockdown of *Tlr2* and *Tlr4* showed similar effects, although to a lesser extent (Extended Data Fig. 7i,j). We then deleted *Neu1* specifically in the myeloid cells of mice ($Neu1^{-/-}$) (Fig. 4j and Extended Data Fig. 7k). E-motif failed to upregulate the inflammatory cytokines in macrophages derived from $Neu1^{-/-}$ mice in vitro (Extended Data Fig. 7l,m). We then used 2,3-dehydro-2-deoxy-*N*-acetylneuraminic acid (DANA), a NEU1 inhibitor that binds to its active site through structural complementarity[40], which also significantly attenuated the E-motif-induced increases in cytokines in macrophages in vitro (Extended Data Fig. 7n). For the in vivo experiment, we injected E-motif into control mice ($Neu1^{f/f}$) or $Neu1^{-/-}$ mice twice a week for 16 weeks (Fig. 4j). The weight of mice in the $Neu1^{-/-}$ + E-motif group was similar to that of the vehicle group and significantly lower than that of the $Neu1^{f/f}$ + E-motif group (Fig. 4k). The serological markers of liver dysfunction and inflammatory factors, as well as the degenerative changes in the liver and WAT, were significantly alleviated in the $Neu1^{-/-}$ + E-motif group compared to the $Neu1^{f/f}$ + E-motif group (Fig. 4l–n). To confirm whether myeloid-specific NEU1 controls E-motif-induced T/B cell dysfunction, we analyzed the proportions of these cells and found a significant decrease in the $Neu1^{-/-}$ + E-motif group compared to the $Neu1^{f/f}$ + E-motif group (Fig. 4o). Transplantation of T/B cells from $Neu1^{-/-}$ mice treated with E-motif or vehicle into recipient Rag mice did not result in any difference in lifespan (Extended Data Fig. 8a,b).

Together, these findings identify monocyte/macrophage-specific NEU1 as a key mediator of the E-motif-induced changes in the frequencies and functions of T/B cells, which consequently promote systemic aging.

NEU1 inhibitor extends healthspan and lifespan and possesses potential translational value

Given the crucial role of NEU1 in E-motif-induced immune dysfunction and the aging process, we investigated the potential role of the NEU1 inhibitor DANA in counteracting the effects of E-motif and delaying natural aging (Extended Data Fig. 8c). DANA attenuated the E-motif-induced increases in body weight (Extended Data Fig. 8d), T/B cells (Extended Data Fig. 8e), serological hepatic markers (Extended Data Fig. 8f) and proinflammatory cytokines (Extended Data Fig. 8g) in mice. Also, DANA effectively mitigated the pro-aging effects of T/B cells transferred from E-motif-treated mice to Rag mice (Extended Data Fig. 8h). Interestingly, DANA did not immediately decrease the serum levels of ELN fragments, although long-term treatment led to a gradual decline (Extended Data Fig. 8i), further confirming that DANA blocks the downstream signals of ELN fragments.

Considering the positive correlation between ELN fragments and age, we evaluated the effects of DANA in wild-type (WT) naturally aged mice without E-motif treatment (Fig. 5a). DANA administration significantly increased the lifespan of both male (by 17.4% for median lifespan) and female (by 12.2% for median lifespan) mice (Fig. 5b and Extended Data Fig. 9a,b). To assess healthspan, body weight was continuously monitored, and other indicators were measured after 24 weeks of DANA treatment (at 84 weeks of age). DANA significantly decreased body weight, fat tissue percentage and abdominal fat weight while increasing the lean tissue percentage (Fig. 5c,d and

https://doi.org/10.1038/s43587-025-00961-8

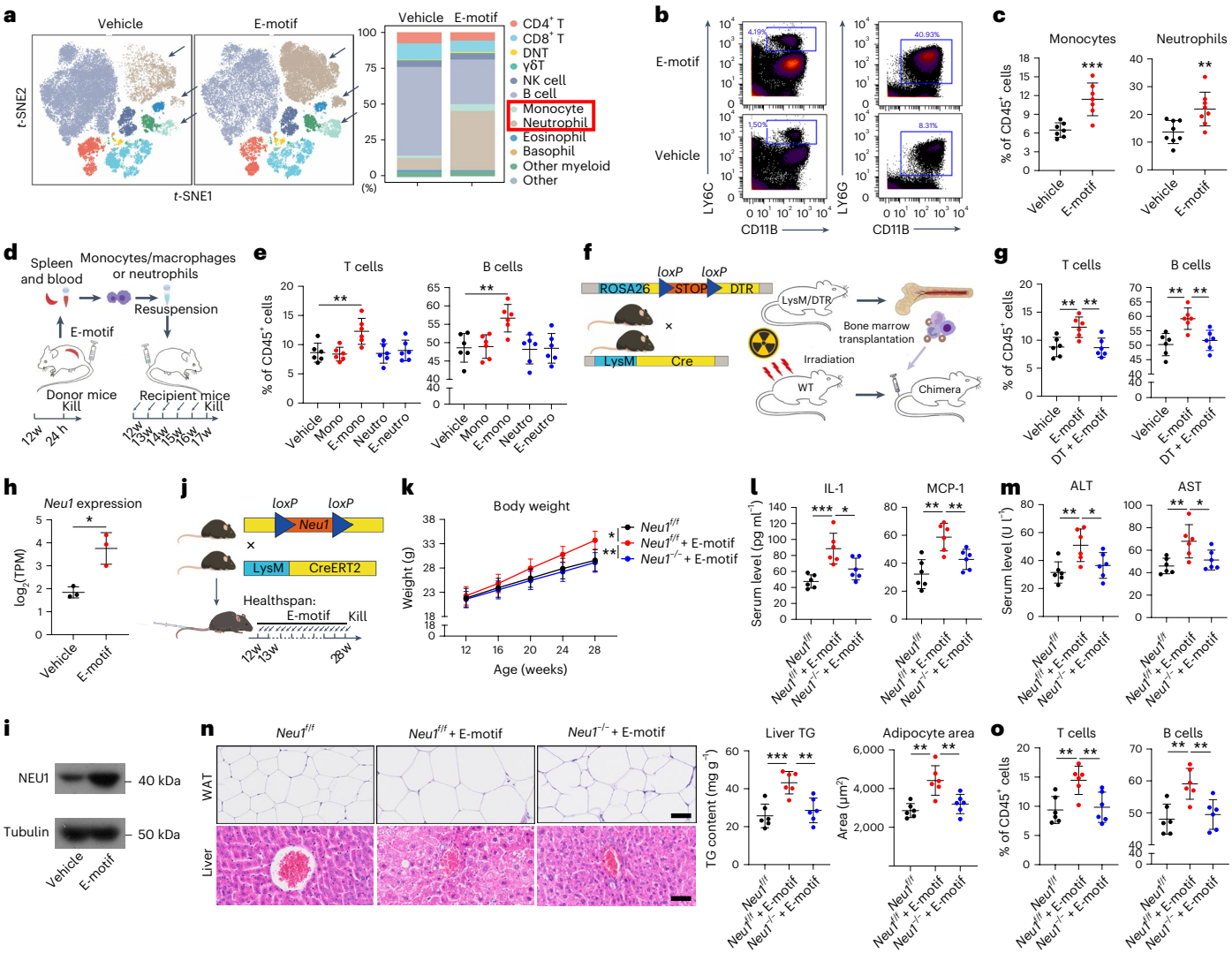

Fig. 4 | Monocytes/macrophages partly mediate the activation of adaptive immunity by E-motif in a NEU1-dependent manner. a, *t*-SNE plot showing cell clusters (left) and quantification of the cell clusters (right), with arrows (left) and the red box (right) highlighting clusters that apparently differ in proportion between the two groups ($n = 5$ per group). DNT, double-negative T cell. **b**, Scatter plot of SPADE analysis illustrating the proportions of cell clusters ($n = 5$ per group). **c**, Flow cytometry analysis of the proportions of monocytes (left) and neutrophils (right) (monocytes: $n = 7$ per group, neutrophils: $n = 8$ per group; monocytes: E-motif versus vehicle $P = 0.0007$, neutrophils: E-motif versus vehicle $P = 0.0067$). **d**, Diagram of cell transplantation using E-motif-injected mice as donors. At 24 h after the injection, different myeloid cells were sorted from donors and transplanted into recipient mice. After five transplantations, recipient mice were killed. **e**, Proportions of T/B cells in the peripheral blood of recipient mice after cell transplantation ($n = 6$ per group; T cells: E-mono versus vehicle $P = 0.0089$, B cells: E-mono versus vehicle $P = 0.0044$). Mono, monocytes; Neutro, neutrophils; E-mono, monocytes from E-motif-treated mice; E-neutro, neutrophils from E-motif-treated mice. **f**, Genotype diagram for LysM/iDTR mice (left) and schematic diagram of chimeric mouse construction (right). **g**, Flow cytometry analysis of the proportions of T/B cells in LysM/iDTR mice ($n = 6$ per group; T cells: E-motif versus vehicle $P = 0.0062$, E-motif versus DT + E-motif $P = 0.0050$; B cells: E-motif versus vehicle $P = 0.0021$, E-motif versus DT + E-motif $P = 0.0047$). **h**,**i**, *Neu1* expression in transcriptomic sequencing data (**h**; $n = 3$ per group; E-motif versus vehicle $P = 0.0104$) and western blot analysis (**i**; $n = 4$ per group). TPM, transcripts per million. **j**, Genotype diagram of mice for the conditional knockout of the *Neu1* gene in myeloid cells and the process of E-motif treatment. **k**, Body weight changes in mice over time ($n = 6$ per group over time; $Neu1^{f/f}$ + E-motif versus $Neu1^{f/f}$ $P = 0.0159$, $Neu1^{f/f}$ + E-motif versus $Neu1^{-/-}$ + E-motif $P = 0.0061$). **l**,**m**, Serum levels of the inflammatory markers IL-1 and MCP-1 (**l**) ($n = 6$ per group; IL-1: $Neu1^{f/f}$ + E-motif versus $Neu1^{f/f}$ $P = 0.0007$, $Neu1^{f/f}$ + E-motif versus $Neu1^{-/-}$ + E-motif $P = 0.0242$; MCP-1: $Neu1^{f/f}$ + E-motif versus $Neu1^{f/f}$ $P = 0.0011$, $Neu1^{f/f}$ + E-motif versus $Neu1^{-/-}$ + E-motif $P = 0.0095$) and the liver function markers ALT and AST (**m**) ($n = 6$ per group; ALT: $Neu1^{f/f}$ + E-motif versus $Neu1^{f/f}$ $P = 0.0065$, $Neu1^{f/f}$ + E-motif versus $Neu1^{-/-}$ + E-motif $P = 0.0385$; AST: $Neu1^{f/f}$ + E-motif versus $Neu1^{f/f}$ $P = 0.0081$, $Neu1^{f/f}$ + E-motif versus $Neu1^{-/-}$ + E-motif $P = 0.0397$). **n**, Representative images of H&E staining of WAT (left top) and liver tissue (left bottom) with quantification of TG content and adipocyte areas (right) ($n = 6$ per group; TG content: $Neu1^{f/f}$ + E-motif versus $Neu1^{f/f}$ $P = 0.0006$, $Neu1^{f/f}$ + E-motif versus $Neu1^{-/-}$ + E-motif $P = 0.0023$; adipocyte area: $Neu1^{f/f}$ + E-motif versus $Neu1^{f/f}$ $P = 0.0011$, $Neu1^{f/f}$ + E-motif versus $Neu1^{-/-}$ + E-motif $P = 0.0085$). **o**, Flow cytometry analysis of the proportions of T/B cells in the peripheral blood ($n = 6$ per group; T cells: $Neu1^{f/f}$ + E-motif versus $Neu1^{f/f}$ $P = 0.0040$, $Neu1^{f/f}$ + E-motif versus $Neu1^{-/-}$ + E-motif $P = 0.0096$; B cells: $Neu1^{f/f}$ + E-motif versus $Neu1^{f/f}$ $P = 0.0025$, $Neu1^{f/f}$ + E-motif versus $Neu1^{-/-}$ + E-motif $P = 0.0056$). $^*P < 0.05$, $^{**}P < 0.01$, $^{***}P < 0.001$. Scale bar, 50 μm for **n**. Statistical tests: unpaired two-tailed Student's *t* test (equal variance) or unpaired two-tailed *t* test with Welch's correction (unequal variance) with a 95% confidence interval (**c**, **e**, **g**–**h**, **l**–**o**); two-way ANOVA (**k**). Data are presented as mean values ± s.d. (**c**, **e**, **g**–**h**, **k**–**o**). Illustrations in panels **f** and **j** were created using FigDraw.

Extended Data Fig. 9c). The DANA group exhibited reduced spinal curvature (Fig. 5e), reduced P16 signal (Fig. 5f), enhanced spontaneous locomotor activity (Fig. 5g,h), improved motor endurance (Fig. 5i) and enhanced grasping ability (Extended Data Fig. 9d) compared to the vehicle group. Blood biochemistry assays showed that DANA significantly alleviated the age-related increases in markers of liver impairment (AST and ALT), hyperglycemia (GLU) and dyslipidemia (LDL and TG) (Fig. 5j,k and Extended Data Fig. 9e,f). DANA treatment also reduced the age-related expression of multiple inflammatory cytokines, indicating its ability to suppress systemic inflammaging (Fig. 5l). The age-related increase in adipocyte area, decrease in epidermal thickness, decrease in muscle fiber area, and fatty degeneration of the liver were all significantly delayed by DANA (Fig. 5m–o and Extended Data Fig. 9g). However, the effects of DANA on bone tissue were modest (Extended Data Fig. 9h). Similarly, DANA did not decrease the serum content of ELN fragments immediately but did decrease the content during the slowed aging process (Extended Data Fig. 9i).

Next, the synergistic effects of combining DANA with other anti-aging interventions were investigated. We administered DANA and the well-established anti-aging drug rapamycin (Fig. 5p). Notably, the coadministration of DANA and rapamycin (DANA + R) exhibited superior efficacy compared to either monotherapy. This was remarkably demonstrated in lifespan extension (Fig. 5q), body weight decrease (Fig. 5r), fat/lean tissue preservation (Extended Data Fig. 9j,k), decreased concentration of hepatic markers (AST and ALT) (Extended Data Fig. 9l), reduced systemic inflammation (IL-1 and MCP-1 levels) (Fig. 5s) and enhanced locomotor activity (Extended Data Fig. 9m). Tissue-level improvements were also more pronounced, with greater muscle fiber increase, more significant WAT adipocyte shrinkage and further hepatic TG reduction (Fig. 5t,u and Extended Data Fig. 9n). Both monotherapies showed similar effects, but each to a lesser extent (Fig. 5p–u and Extended Data Fig. 9j–n). These results demonstrate the enhanced anti-aging benefits of combined administration of DANA and rapamycin.

To further validate the effects of DANA, we conducted a study in a large animal model (Yorkshire pigs) (Fig. 6a). The pigs were treated with PBS (vehicle), E-motif, or a combination of E-motif and DANA (E-motif + DANA) twice a week for 16 weeks. Blood biochemistry analysis showed that, compared to the E-motif group, the E-motif + DANA group exhibited significant improvements in markers of liver function, including AST, alkaline phosphatase (ALP) and albumin (ALB) levels. DANA also improved metabolic indicators, including GLU, TG and LDL, as well as markers of kidney function, such as blood urea nitrogen (BUN) and creatinine (CREA) levels (Fig. 6b). Similar results were observed in immune-humanized mice injected with vehicle, human ELN fragments (ELN group) or ELN + DANA (Fig. 6c). At the end of the experiment, the ELN + DANA group showed normalized levels of AST, ALP, ALB, GLU, TG, LDL, BUN and CREA (Fig. 6d). Together, these results suggest that DANA effectively mitigates E-motif- or ELN fragment-induced physiological dysfunctions across species, including in a large mammal model and humanized mice.

We finally analyzed 1,068 human serum samples to investigate the relationship between ELN fragment content and various health indicators in the same cohort shown in Fig. 1a. Linear regression analysis demonstrated a strong correlation between ELN fragment content and age (Fig. 6e). Data from the total cohort and specific age groups indicated that the concentrations of ELN fragments were notably positively correlated with markers of obesity (body mass index (BMI)), hypertension (systolic blood pressure (SBP) and diastolic blood pressure (DBP)), liver function abnormalities (AST, gamma-glutamyl transferase, ALP, total protein and bilirubin), dyslipidemia (TG, LDL, high-density lipoprotein and total cholesterol) and renal dysfunction (estimated glomerular filtration rate, urea and CREA). The concentrations of ELN fragments were also positively correlated with chronic inflammation, hyperglycemia, hyperuricemia and thyroid hyperfunction (Fig. 6f). In a comparison between the normal and high ELN groups, the high ELN group exhibited significantly impaired BMI, SBP, DBP, AST, ALP, ALB, TG, LDL, urea, CREA and GLU levels (Fig. 6g,h), confirming that high serum levels of ELN

Fig. 5 | DANA, as a NEU1 inhibitor, extends healthspan and lifespan. **a**, Schematic diagram illustrating the experimental design of intraperitoneally (i.p.) injecting DANA into mice to study its effects on healthspan and lifespan. **b**, Survival curves of male mice (vehicle: $n = 25$, DANA: $n = 24$; DANA versus vehicle: $P < 0.0001$ by log-rank test and $P < 0.0001$ by Gehan–Breslow–Wilcoxon test). **c**, Time-series analysis of body weight ($n = 11$ per group over time, but $n = 10$ for the vehicle group at 80 and 84 weeks; DANA versus vehicle: at 80 weeks $P = 0.0133$, at 84 weeks $P = 0.0087$). **d**, Analysis of the percentages of fat tissue (left) and lean tissue (right) relative to body weight at the experimental endpoint (84 weeks of age) ($n = 10$ per group; fat tissue: DANA versus vehicle $P = 0.0010$, lean tissue: DANA versus vehicle $P = 0.0378$). **e**, Representative X-ray images of mice, with black lines indicating the basis for kyphosis index calculation (left), and quantification of the kyphosis index (right) ($n = 6$ per group; DANA versus vehicle $P = 0.0274$). **f**, *P16* gene expression pattern in P16-3MR mice (top), along with in vivo bioluminescence imaging (bottom left) and quantification (bottom right) ($n = 4$ per group; DANA versus vehicle $P = 0.0445$). **g**, Movement trajectories of mice in the open field test. **h**, Total movement distance (left) and average speed (right) ($n = 6$ per group; total movement distance: DANA versus vehicle $P = 0.0025$, average speed: DANA versus vehicle $P = 0.0026$). **i**, Treadmill test schematic (left) and analysis of the number of electric shocks administered (right) ($n = 9$ per group; DANA versus vehicle $P = 0.0084$). **j**, Schematic representation of serum extraction from peripheral blood samples. **k**, Serum levels of AST and ALT ($n = 7$ per group; AST: DANA versus vehicle $P = 0.0044$, ALT: DANA versus vehicle $P = 0.0347$). **l**, Heatmap depicting the levels of serum inflammatory markers, with fold changes relative to the mean values of the vehicle group ($n = 5$ per group). **m**, Representative images of H&E staining of WAT (left) and quantification of the adipocyte area (right) (vehicle: $n = 6$, DANA: $n = 7$; DANA versus vehicle $P = 0.0005$). **n**, Representative images of H&E staining of skin tissue (left) and quantification of epidermal thickness (right) ($n = 7$ per group; DANA versus vehicle $P < 0.0001$). **o**, Representative images of H&E staining of liver tissue (left) and quantification of TG content (right) ($n = 7$ per group; DANA versus vehicle $P < 0.0001$). **p**, Schematic diagram illustrating the experimental design of the study investigating the synergistic effects of DANA with rapamycin (R). **q**, Survival curves of mice injected with vehicle, DANA, R and DANA + R (vehicle: $n = 12$; DANA, R, DANA + R: $n = 13$; DANA + R versus vehicle: $P < 0.0001$ by log-rank test and $P = 0.0003$ by Gehan–Breslow–Wilcoxon test, DANA + R versus DANA: $P = 0.0205$ by log-rank test and $P = 0.0225$ by Gehan–Breslow–Wilcoxon test, DANA + R versus R: $P = 0.0406$ by log-rank test and $P = 0.0546$ by Gehan–Breslow–Wilcoxon test). **r**, Body weight changes in mice over time ($n = 6$ per group; DANA + R versus vehicle: at 76 weeks $P = 0.0015$, at 80 weeks $P = 0.0008$, at 84 weeks $P < 0.0001$). **s**, Serum levels of the inflammatory markers IL-1 and MCP-1 ($n = 6$ per group; IL-1: DANA + R versus vehicle $P = 0.0002$, DANA + R versus R $P = 0.0062$, DANA + R versus DANA $P = 0.0386$; MCP-1: DANA + R versus vehicle $P = 0.0007$, DANA + R versus R $P = 0.0073$, DANA + R versus DANA $P = 0.0035$). **t**, Representative images of H&E staining of liver tissue (left) with quantification of TG content (right) ($n = 6$ per group; DANA + R versus vehicle $P = 0.0005$, DANA + R versus R $P = 0.0022$, DANA + R versus DANA $P = 0.2455$). **u**, Representative images of H&E staining of WAT (left) with quantification of the adipocyte area (right) ($n = 6$ per group; DANA + R versus vehicle $P = 0.0003$, DANA + R versus R $P = 0.0485$, DANA + R versus DANA $P = 0.0055$). $^*P < 0.05$, $^{**}P < 0.01$, $^{***}P < 0.001$, $^{****}P < 0.0001$. Scale bar, 50 μm for **m**, **n**, **o**, **t** and **u**. Statistical tests: log-rank test and Gehan–Breslow–Wilcoxon test (**b**); two-way ANOVA (**c**, **r**); unpaired two-tailed Student's *t* test (equal variance) or unpaired two-tailed *t* test with Welch's correction (unequal variance) with a 95% confidence interval (**d**–**f**, **h**–**k**, **m**–**o**); one-way ANOVA with Bonferroni post hoc test (**s**–**u**). The dashed line in bar plots represents the average values for middle-aged mice (36 weeks old). Data are presented as mean values ± s.d. (**c**–**f**, **h**–**k**, **m**–**o**, **r**–**u**). Illustrations in panels **a** and **p** were created using FigDraw.

https://doi.org/10.1038/s43587-025-00961-8

fragments are a risk factor for aging-related disorders. In human macrophages in vitro, DANA could alleviate the upregulation of inflammatory factors induced by human serum with high ELN fragment content (Extended Data Fig. 10).

Therefore, DANA extends healthspan and lifespan in WT mice and mitigates the pro-aging effects of E-motif in both WT mice and pigs, as well as the effects of human ELN fragments in humanized mice. Moreover, ELN fragments are correlated with numerous aging markers

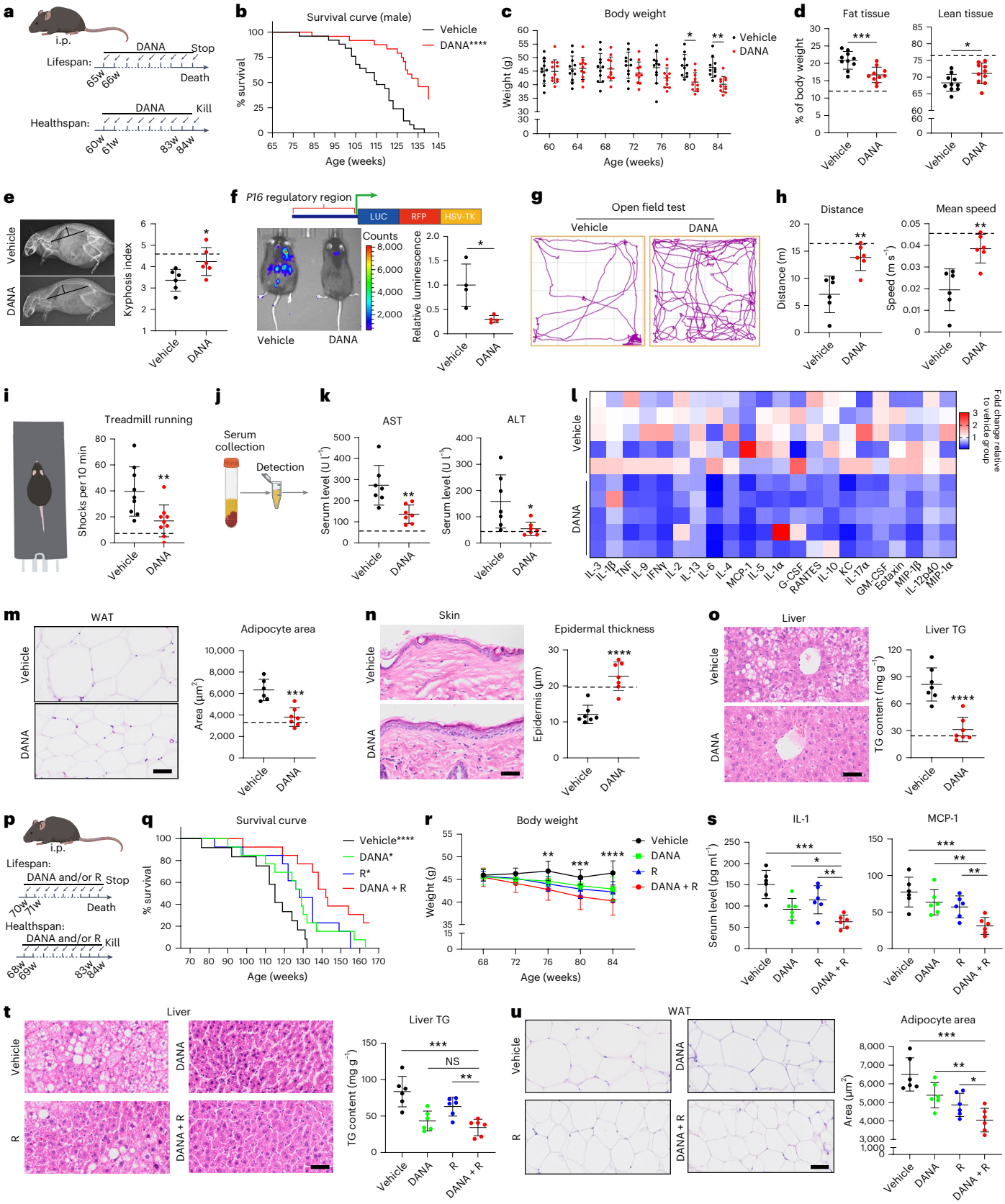

https://doi.org/10.1038/s43587-025-00961-8

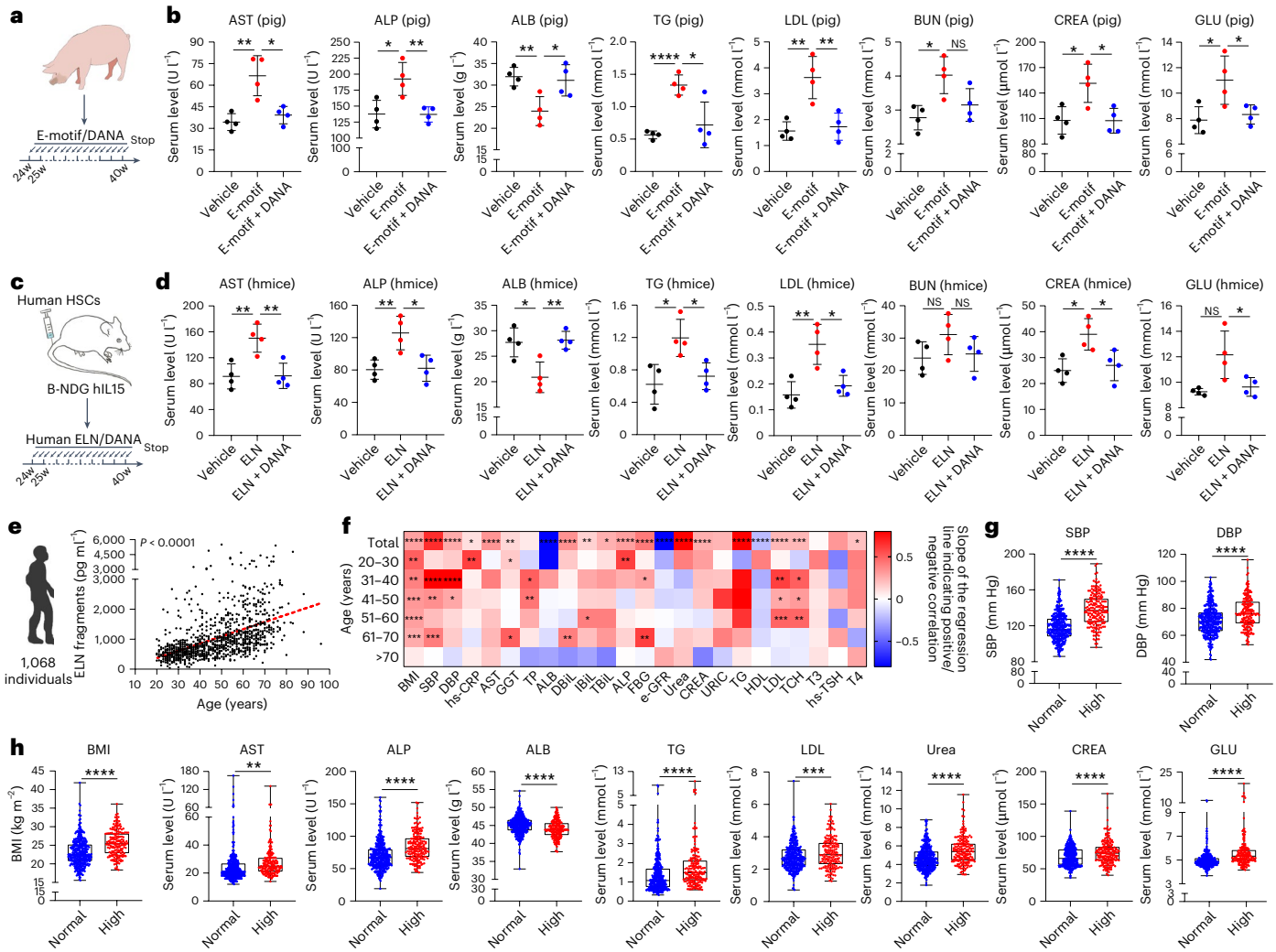

Fig. 6 | Potential clinical values of ELN fragments and DANA. a, Schematic diagram illustrating the experimental design of the study investigating the effects of DANA on E-motif-induced aging in Yorkshire pigs. **b**, Serum levels of AST, ALP, ALB, TG, LDL, BUN, CREA and GLU in the pig model ($n = 4$ per group; AST: E-motif versus vehicle $P = 0.0053$, E-motif + DANA versus E-motif $P = 0.0113$; ALP: E-motif versus vehicle $P = 0.0169$, E-motif + DANA versus E-motif $P = 0.0078$; ALB: E-motif versus vehicle $P = 0.0071$, E-motif + DANA versus E-motif $P = 0.0279$; TG: E-motif versus vehicle $P < 0.0001$, E-motif + DANA versus E-motif $P = 0.0188$; LDL: E-motif versus vehicle $P = 0.0035$, E-motif + DANA versus E-motif $P = 0.0078$; BUN: E-motif versus vehicle $P = 0.0086$; CREA: E-motif versus vehicle $P = 0.0195$, E-motif + DANA versus E-motif $P = 0.0167$; GLU: E-motif versus vehicle $P = 0.0277$, E-motif + DANA versus E-motif $P = 0.0385$). **c**, Illustration of the construction of an immune-humanized mouse model and experimental design of the study investigating the effects of DANA on E-motif-induced aging in immune-humanized mice. HSCs, hematopoietic stem cells. **d**, Serum levels of AST, ALP, ALB, TG, LDL, BUN, CREA and GLU in the immune-humanized mouse model (hmice) ($n = 4$ per group; AST: ELN versus vehicle $P = 0.0067$, ELN + DANA versus ELN $P = 0.0073$; ALP: ELN versus vehicle $P = 0.0091$, ELN + DANA versus ELN $P = 0.0162$; ALB: ELN versus vehicle $P = 0.0161$, ELN + DANA versus ELN $P = 0.0057$; TG: ELN versus vehicle $P = 0.0143$, ELN + DANA versus ELN $P = 0.0156$; LDL: ELN versus vehicle $P = 0.0056$, ELN + DANA versus ELN $P = 0.0104$; CREA: ELN versus vehicle $P = 0.0101$, ELN + DANA versus ELN $P = 0.0295$; GLU: ELN + DANA versus ELN $P = 0.0454$). **e**, Relationship between the serum content of ELN fragments and age in a human cohort. The red dashed line represents the linear regression line ($n = 1{,}068$; $P < 0.0001$). **f**, Heatmap showing the correlation between the serum levels of ELN fragments and various aging markers or negative health indicators across different age groups in the human population, based on β coefficients from a regression analysis. hs-CRP, high-sensitivity C-reactive protein; GGT, gamma-glutamyl transferase; TP, total protein; DBiL, direct bilirubin; IBiL, indirect bilirubin; TBiL, total bilirubin; FBG, fasting blood glucose; e-GFR, estimated glomerular filtration rate; URIC, uric acid; HDL, high-density lipoprotein; TCH, total cholesterol; T3, triiodothyronine; hs-TSH, high-sensitivity thyroid-stimulating hormone; T4, thyroxine. Red blocks represent a positive correlation (total, $n = 1{,}068$; age 20–30 years, $n = 197$; 31–40 years, $n = 233$; 41–50 years, $n = 187$; 51–60 years, $n = 187$; 61–70 years, $n = 201$; >70 years, $n = 63$). **g**, Statistical analysis of SBP and DBP in the high ELN and normal ELN groups (normal group: $n = 375$, high group: $n = 186$; SBP: normal versus high $P < 0.0001$, DBP: normal versus high $P < 0.0001$). **h**, Statistical analysis of BMI and the serum levels of AST, ALP, ALB, TG, LDL, urea, CREA and GLU in the high ELN and normal ELN groups (BMI: normal group $n = 370$, high group $n = 183$, normal versus high $P < 0.0001$; AST: normal group $n = 401$, high group $n = 187$, normal versus high $P = 0.0061$; ALP: normal group $n = 401$, high group $n = 187$, normal versus high $P < 0.0001$; ALB: normal group $n = 401$, high group $n = 187$, normal versus high $P < 0.0001$; TG: normal group $n = 367$, high group $n = 176$, normal versus high $P < 0.0001$; LDL: normal group $n = 367$, high group $n = 176$, normal versus high $P = 0.0004$; urea: normal group $n = 400$, high group $n = 187$, normal versus high $P < 0.0001$; CREA: normal group $n = 400$, high group $n = 187$, normal versus high $P < 0.0001$; GLU: normal group $n = 401$, high group $n = 187$, normal versus high $P < 0.0001$). In the box plots, the center line denotes the median, the box range indicates the 25th–75th percentile range, and whiskers denote minimum–maximum values (**g**, **h**). $^{*}P < 0.05$, $^{**}P < 0.01$, $^{***}P < 0.001$, $^{****}P < 0.0001$. Statistical tests: Pearson correlation coefficients with a two-tailed 95% confidence interval (**e**, **f**); unpaired two-tailed Student's t test (equal variance) or unpaired two-tailed t test with Welch's correction (unequal variance) with a 95% confidence interval (**b**, **d**, **g**, **h**). Data are presented as mean values ± s.d. (**b**, **d**, **g**, **h**).

or negative health indicators in humans, highlighting the potential clinical value of targeting NEU1 with inhibitors such as DANA to combat aging and age-related diseases.

Discussion

Previous studies have mainly focused on the cellular events during aging, while the role of ECM events has been largely overlooked. Our study investigated the impact of degraded ECM components, known as matrikines, on the aging process. First, we discovered that several matrikines are not only positively correlated with aging in both mice and humans, but they also actively promote aging. Notably, the E-motif of ELN fragments remarkably reduces healthspan and lifespan. Second, we found that E-motif activates monocytes/macrophages, which in turn induce a pro-aging lymphocyte phenotype, thereby accelerating metabolic dysfunctions, leading to unhealthy aging and a shortened lifespan. Third, we identified that NEU1 in monocytes/macrophages partly mediates E-motif-induced immune activation. Remarkably, the NEU1 inhibitor DANA extends healthspan and lifespan in WT naturally aged mice. DANA mitigates the aging indicators induced by E-motif and human ELN fragments in pig and humanized mouse models, respectively. Our study opens up a new area of research focusing on the role of the degradative ECM in aging and provides a new anti-aging intervention strategy targeting matrikine signaling.

First, we revealed a 'self-propelled vicious circle' involving several matrikines during systemic aging, with a particular emphasis on ELN fragments. Previous studies have reported that the serum levels of ELN fragments are increased during several degenerative diseases and correlate with negative health markers, including atherosclerosis, hypertension[3,4,41], COPD[5], fatty liver disease[42], and elevated levels of BMI as well as the serological markers TG, C-reactive protein, GLU and insulin[41,42]. Our analysis of a large cohort comprising 1,068 individuals, which is substantially larger than the sample size in previous studies (typically ≤200), confirmed similar results regarding hypertension, BMI, and serum levels of TG, high-sensitivity C-reactive protein and GLU. Additionally, our study demonstrates that the ELN fragment content correlates with several serological markers of liver and kidney degeneration, as well as with other markers of dyslipidemia (LDL, high-density lipoprotein and total cholesterol) and mild thyroid dysfunction. Previous studies on the effects of ELN fragments in mice primarily focused on COPD[14], metabolic dysfunction-associated steatohepatitis[42], hyperglycemia[43] and vascular disease[44]. Our findings align with these studies, revealing significant hepatic steatosis, hyperglycemia and other metabolic disturbances after treatment with ELN fragments. However, in contrast to previous studies that used relatively high doses of ELN fragments for a short duration (for example, 10 mg kg^{-1} weekly for 8 weeks)[42], we administered E-motif at a lower dose (150 μg kg^{-1})—based on our detection of physiological concentrations—for an extended period (twice a week for 24 weeks) to mimic the aging process. Notably, even collected endogenous ELN fragments led to aging-related immunological and metabolic dysfunction. Our study reveals that ELN fragments, particularly the E-motif, shorten lifespan and induce several indicators of aging. As fragments of other ECM components (such as HA and FN) also reduce healthspan and lifespan, although to a lesser extent, matrikines could be crucial drivers and/or markers of aging. These findings supplement previous aging-related knowledge[2].

Our study also elucidated the immunological mechanisms underlying E-motif-induced metabolic dysfunction and systemic aging, providing a new explanation for age-related immune dysfunction and inflammation caused by matrikines. The T/B cell deletion and transplantation model demonstrated that T/B cells partly mediate the E-motif-induced shortening of healthspan and lifespan. The degeneration of the entire immune system or T cells alone can induce systemic chronic inflammation, aging and a shorter lifespan[19,20]. Specifically, $CD8^+GZMK^+$ Tc and $CD4^+IFN\gamma^+$ T_H1 cells have been reported to be directly related to inflammaging[33,45,46]. After long-term E-motif treatment, the T cells in our model could promote aging by skewing similar subclusters and causing molecular changes. Our study further found that the effects of E-motif on T/B cells are partly mediated by monocytes/macrophages. Although the frequency of neutrophils is increased, they do not participate in the activation of lymphocytes. A previous study revealed that neutrophils show a lesser response to ELN fragments than monocytes[47], partially explaining why neutrophils are not the main cells involved. More importantly, a previous study reported that MHC-II and antigen-processing cells are indispensable for the activation of lymphocytes by ELN fragments in individuals with smoking-induced emphysema and smokers with thoracic aortic aneurysm and dissection[48,49]. Our RNA-seq data in monocytes/macrophages revealed the upregulation of pathways related to antigen-processing and inflammation. Monocytes/macrophages may, at least in part, have a role in antigen processing. In addition, the inflammatory factors induced by monocytes/macrophages could contribute to the activation of lymphocytes, as the presence of antigen-processing cells alone is insufficient[48,49].

Finally, we revealed that NEU1 inhibition extends healthspan and lifespan in several models. Previous studies reported that the NEU1 inhibitor DANA blocks ELN fragment-induced reactive oxygen species production and migration in monocytes[15] and the uptake of LDL (a trigger of inflammatory responses and atherosclerosis) in macrophages[50]. Similarly, we revealed that the knockdown, knockout or inhibition of NEU1 by DANA in macrophages blocks the secretion of inflammatory factors induced by ELN fragments. Previous studies reported that DANA blocks hyperglycemia and metabolic dysfunction-associated steatohepatitis induced by ELN fragments[42,43]. In a mouse model of E-motif-induced aging, we extended previous knowledge by revealing the effects of NEU1 knockout and DANA on reversing abnormal immunological activation, metabolic dysfunction and consequent lifespan shortening. Using a naturally aging model, we clarified that DANA improves lifespan, motor ability, kyphosis index, and obesity- and skin-related indicators, demonstrating synergistic effects with rapamycin. We further confirmed the beneficial effects of DANA in pigs, humanized mice and human cells, indicating that the role of DANA and the interaction between NEU1 and ELN fragments are conserved. Notably, DANA shares the parent scaffold of several Food and Drug Administration-approved drugs, including zanamivir and oseltamivir[51], highlighting its promising translational value for interventions targeting aging and age-related diseases.

There are some limitations to this study that may serve as future avenues for research. First, our results indicate that HA fragments moderately accelerate aging, while FN fragments have a slight effect and COL fragments do not accelerate aging. The FN and COL fragments used in this study are only some of their degraded products, which increase with age according to our findings. Further investigation is needed to determine whether other domains (motifs) of FN and COL fragments can induce systemic aging. Second, we clarified that immune dysfunction and NEU1 in monocytes/macrophages have important roles in E-motif-induced systemic aging. However, *Neu1* is expressed not only in immune cells but also in other tissues, such as the kidneys and heart, and its upregulation can mediate the development of fibrotic kidneys and cardiac hypertrophy[35,36]. Therefore, it is possible that immune dysfunction has a partial role, and other *Neu1*-expressing cells may contribute to the pro-aging effects of E-motif. Third, metabolic dysfunction, increased body weight and WAT-related changes were widely observed in animal models of E-motif treatment and in a human cohort with high ELN content. As chronic inflammation, WAT changes and metabolic dysfunction show widely reciprocal regulation during aging[31,52,53], further studies could focus on the roles of these factors in E-motif-induced aging.

Methods

Ethical approval

The detection and analysis of clinical samples in this study were conducted under the ethical approval of the Fourth Affiliated Hospital Zhejiang University School of Medicine (K2022171). The cohort was established in Yiwu, Zhejiang Province, China. Registration was performed, and written informed consent was obtained. Animal experiments were conducted with the approval of the Zhejiang University Experimental Animal Welfare and Ethics Committee in accordance with Institutional Animal Care and Use Committee guidelines (ZJU20230096 for mouse experiments, ZJU20240053 for pig experiments).

Animal strains

Male animals were used unless otherwise stated. WT C57BL/6J mice (GemPharmatech and SLAC Laboratory Animal) were used in the majority of the experiments in this study. P16-3MR mice, which have a luciferase gene knocked in under the control of the *P16* regulatory region[29], were generously donated by J. Campisi (Buck Institute for Research on Aging, USA). LysM-Cre mice and ROSA26-STOP-iDTR mice were generously donated by W. Shen (Zhejiang University, China) and W.B. Gan (Peking University, Shenzhen Graduate School, China), respectively. Homozygous LysM-Cre mice and homozygous ROSA26-STOP-iDTR mice were crossed to obtain LysM/iDTR mice, which express the diphtheria toxin (DT) receptor (DTR) in myeloid cells[54]. LysM-Cre mice were crossed with *Neu1*-flox mice (NM-CKO-2100114, Shanghai Model Organisms) to obtain LysM-Cre/*Neu1*-flox mice. The mice used in this study were LysM-Cre heterozygous and *Neu1*-flox homozygous for the conditional knockout of the *Neu1* gene. Immune-humanized mice were purchased from Biomice (112478). Briefly, B-NDG hIL15 mice were adoptively transferred with human $CD34^+$ cells. These mice exhibited humanized cells including lymphocytes, natural killer cells and monocytes[55,56]. *Rag1*-knockout mice, which lack mature T/B cells, were obtained from GemPharmatech (T004753). Mice were housed with no more than five per cage under a 12-h light–dark cycle at a temperature of 21–25 °C and a humidity of 45–55% and were fed a standard chow diet (Xietong Shengwu, XTI01FZ). Mice had access to food and water ad libitum.

ECM fragments

ELN fragments were purchased from Elastin Products Company (MLP45). They were prepared by enzymatic hydrolysis of mouse lung ELN using mouse pancreatic elastase and then purified. HA fragments were obtained from Bloomage Biotechnology (20071451). They were derived from low-molecular-weight HA and produced by microbial fermentation. FN fragments were purchased from Novoprotein (CH38). These are recombinant human FN fragments containing the sequences Pro1270–Ser1546 and Ala1721–Thr2016, a central cell-binding domain, a high-affinity heparin-binding domain II and a CS1 site within the alternatively spliced III CS region[57]. They were produced by microbial fermentation. COL fragments were purchased from Scierbio, produced by solid-phase peptide synthesis. The sequence is EKAHDGGR, a carboxyl-terminal peptide of type I COL that is a marker of degenerative musculoskeletal diseases in mice and humans[58–60]. ELN is a conserved protein between mice and humans. E-motif (sequence: VGVAPGVGVAPG), the corresponding scrambled peptide (sequence: VVGPGAVVGPGA) and poly(A/K) (sequence: AAAAAAKAAAKAAK) were obtained from Scierbio, produced by solid-phase peptide synthesis. This information is also listed in Supplementary Table 1.

Animal experiments

Supplementary Table 2 lists the animal strains, the exact sample size (n) of each group, the cohort, the starting age and the experimental period for the animal experiments. Detailed information is also described below.

For exploring which kind of matrikine (ECM-derived fragments) showed the most potent pro-aging effects, all matrikines were delivered to mice through tail vein injection, twice a week on the first and fourth days of each week due to the generally short half-life of drugs administered through this route[61–63] (Supplementary Fig. 2). At each injection, according to their physiological concentration in serum, matrikines were dissolved in sterile 50 µl DPBS (14190250, Thermo Fisher Scientific), with the injection doses as follows: ELN fragments, 500 µg kg^{-1}; HA fragments (low-molecular-weight HA), 100 mg kg^{-1}; FN fragments, 5 mg kg^{-1}; COL fragments, 10 µg kg^{-1}. To investigate the effect of matrikines on lifespan, we started the injections at 40 weeks postnatally and stopped when 50% of the mice in the shortest-lifespan group had died. To explore the effects of matrikines on healthspan (that is, other aging indicators), we treated the mice from the 12th week to the 36th week, for a total of 48 injections.

To explore whether endogenous ELN fragments have a role in promoting aging, we collected ELN fragments from the serum of aged mice (older than 84 weeks) and young mice (12 weeks old) using an anti-ELN antibody[64] (Sigma, E4013, BA-4, 5 mg kg^{-1}) and injected the ELN fragments into young mice (12 weeks old). Briefly, the complex of protein A/G magnetic beads and anti-ELN antibody (Sigma, E4013, BA-4, 5 mg kg^{-1}) was added to mouse serum and incubated overnight at 4 °C. The beads were then washed three times with 500 µl of 1× TBS, and the antigen–antibody complexes were retained using a magnetic rack. ELN fragments were eluted with 0.1 mol l^{-1} glycine–HCl (incubated at room temperature for 5 min). The eluate was separated using a magnetic rack, and 0.5 mol l^{-1} Tris–HCl was added to neutralize the solution. ELN fragments were collected from the serum of either >20-month-old (old) or 3-month-old (young) mice. We injected 150 µg kg^{-1} ELN fragments collected from old mice (ECO group) and an equal volume (an equal amount was obtained from young mice, but with a lower concentration because ELN fragments increase with age) of ELN fragments collected from young mice (ECY group) as a control through tail vein injection. This was administered twice a week from the 12th to the 28th week, totaling 32 injections. Mice were divided into three groups: (1) vehicle group (receiving the eluate without serum incubation), (2) ECY group and (3) ECO group. To further demonstrate that it is the collected ELN fragments and not other potential impurities that induce aging, we administered ECO intravenously, combined with the intraperitoneal administration of either 5 mg kg^{-1} BA-4 anti-ELN antibody or IgG control, twice a week from the 12th to the 28th week. Mice were divided into two groups: (1) ECO + IgG and (2) ECO + anti.

To investigate the impact of cellular senescence on the generation of ELN fragments, we treated mice with the senolytic agents dasatinib (5 mg kg^{-1} per day) and quercetin (50 mg kg^{-1} per day) (D + Q) in vehicle (60% PBS, 10% ethanol, 40% PEG-400) through oral gavage. The senolytic cocktail was administered daily for three consecutive days every 2 weeks, with this cyclic treatment protocol starting from the 70th week and maintained over a 14-week experimental period. The mice were divided into three groups: young (12 weeks old), old and old D + Q. The old group received vehicle alone following identical protocols. After treatment, the ELN fragments in serum were detected by ELISA, as described in 'ELISA and blood biochemical testing' in the Methods. Neutrophils and macrophages were separated to quantify $P16^{INK4A}$ expression and measure the NE and ME contents, respectively, using ELISA, as described in 'ELISA and blood biochemical testing' in the Methods. To determine whether the inhibition of NE and ME could reduce ELN fragments in the serum of old mice (84 weeks old), the mice were treated with 5 mg kg^{-1} of an NE inhibitor (S7198, Sigma-Aldrich) intraperitoneally for seven consecutive days or 5 mg kg^{-1} of an ME inhibitor (444291, Sigma-Aldrich) orally for seven consecutive days.

To explore whether specific motifs enriched in ELN fragments, such as E-motif and poly(A/K), shorten lifespan, we dissolved 150 µg kg^{-1} oligopeptides in sterile 50 µl DPBS and delivered them to mice by tail vein injection twice a week, on the first and fourth days of each week. The injection was started at 40 weeks postnatally and stopped when 50% of the mice in the shortest-lifespan group had died. In experiments

assessing healthspan, only E-motif was used because poly(A/K) was not observed to cause lifespan shortening. E-motif was injected at the same frequency and dose as used in the lifespan tests, starting from the 12th week to the 36th week, for a total of 48 injections. For the evaluation of E-motif-induced P16 bioluminescence, P16-3MR mice were administered the treatment at the same frequency and dose. We also used a scrambled oligopeptide to investigate its pro-aging effects as a control for the E-motif. The treatment protocol for the scrambled oligopeptide was identical to that for the E-motif.

To explore long-term immunological changes induced by E-motif, we analyzed immune cells, tissues and organs after treating mice with 150 μg kg^{-1} E-motif through tail vein injection twice a week from the 12th week to the 36th week, totaling 48 injections. PBMCs were extracted for CyTOF (described in 'Cytometry by time-of-flight' in the Methods) and flow cytometry (described in 'Flow cytometry' in the Methods) analyses, and splenocytes were extracted for single-cell RNA-seq (described in 'RNA extraction, sequencing and analysis' in the Methods).

To explore the roles of lymphocytes in E-motif-induced lifespan shortening in *Rag1*$^{-/-}$ mice (Rag mice), we injected the mice with 150 μg kg^{-1} E-motif through the tail vein twice a week from the 30th week. The injections were stopped when 50% of the mice in the shortest-lifespan group had died. Lymphocyte transplantation (described in 'Fluorescence-activated cell sorting and cell transplantation' in the Methods) was performed twice, at 29 and 50 weeks. To explore the roles of lymphocytes in E-motif-induced healthspan shortening in Rag mice, we injected the mice with 150 μg kg^{-1} E-motif twice a week from the 8th week to the 24th week, for a total of 48 injections. Lymphocyte transplantation was performed once on the 7th week.

To explore short-term immunological changes induced by E-motif, we injected 150 μg kg^{-1} E-motif only once into 12-week-old mice through the tail vein. At 24 h after the injection, multiple organs and peripheral blood samples were collected for further analysis.

To explore the roles of myeloid cells in E-motif-induced changes in lymphocytes, we used two mouse models. First, we transplanted myeloid cells (monocytes/macrophages or neutrophils) from E-motif-treated mice to receptor WT mice (described in 'Fluorescence-activated cell sorting and cell transplantation' in the Methods). Donor mice (12 weeks old) were injected with 300 μg kg^{-1} E-motif once. At 24 h after the injection, the donor mice were killed. Monocytes/macrophages or neutrophils were sorted from the spleen and PBMCs and injected into 12-week-old recipient mice once a week for five weeks. Five weeks after the first cell injection, recipient mice were killed, and the lymphocytes in PBMCs were detected. The experiments were divided into five groups (vehicle, mono, E-mono, neutro and E-neutro) based on whether the donor mice were treated with E-motif and the type of cells transplanted. Second, we used chimeric LysM/iDTR mice to delete monocytes/macrophages (described in 'Conditional gene knockout and cell deletion' in the Methods). E-motif was injected at a dose of 150 μg kg^{-1} through the tail vein of 24-week-old mice, twice a week for a total of ten times. Mice were killed 5 weeks after the first injection, and the lymphocytes in PBMCs were detected.

To demonstrate that blocking the inflammatory processes induced by E-motif directly influences the aging process, we first revealed in Supplementary Fig. 7a that IL-1β, IL-6, RANTES (also known as CCL5) and MIP-1α (also known as CCL3) were consistently or obviously upregulated by E-motif. We then screened which of these factors had an important role in the upregulation of lymphocytes. In this experiment, 150 μg kg^{-1} E-motif was injected through the tail vein of 12-week-old mice, twice a week for a total of ten times. Mice were killed 5 weeks after the first injection, and the percentages of lymphocytes in white blood cells were measured by the Safety Assessment Center of Zhejiang University using a Mindray BC-5800 automated hematology analyzer (Mindray Bio-Medical Electronics Equipment). After confirming that IL-1β, IL-6 and MIP-1α have important roles in the upregulation of lymphocytes, we investigated whether blocking these factors could alleviate E-motif-induced aging by using a combination of antibodies to IL-1β (R&D Systems, MAB401, 5 mg kg^{-1}), IL-6 (R&D Systems, MAB406, 2 mg kg^{-1}) and MIP-1α (R&D Systems, AF-450, 2 mg kg^{-1}). In this experiment, 12-week-old mice were injected with 150 μg kg^{-1} E-motif through the tail vein, twice a week for 16 weeks. The combination of the three antibodies or control IgG was intraperitoneally injected simultaneously with the E-motif injection.

To determine the roles of *Neu1* in myeloid cells in E-motif-induced aging, we used LysM-Cre/*Neu1*-flox mice, in which *Neu1* was deleted in myeloid cells (described in 'Conditional gene knockout and cell deletion' in the Methods). The 12-week-old mice were injected with 150 μg kg^{-1} E-motif through the tail vein, twice a week for 16 weeks.

For the investigation of the roles of the NEU1 inhibitor DANA (GC44298, GlpBio) in alleviating natural aging in mice, DANA was dissolved in DPBS and intraperitoneally injected at a dose of 2.5 mg kg^{-1} once a week. In the lifespan evaluation, DANA was injected from week 65 until the mice died. In the healthspan evaluation, DANA was intraperitoneally injected once a week starting from week 60, for a total of 24 injections. To explore P16 bioluminescence after DANA treatment, we injected naturally aged P16-3MR mice with the same frequency and dose.

To investigate the synergistic anti-aging effects of DANA and rapamycin (HY-10219, MCE), we designed four experimental groups: DANA, rapamycin (R), DANA + R and vehicle. DANA was dissolved in DPBS and intraperitoneally injected at a dose of 2.5 mg kg^{-1} once a week. Rapamycin was reconstituted in ethanol at a concentration of 10 mg ml^{-1} and subsequently diluted in 5% Tween-80 (P4780, Sigma) and 5% PEG-400 (P103737, Aladdin). It was administered intraperitoneally at a dose of 6 mg kg^{-1} once a week. In the DANA + R group, both 2.5 mg kg^{-1} DANA and 6 mg kg^{-1} rapamycin were injected intraperitoneally. The vehicle group received intraperitoneal injections of DPBS at the same dose as the DANA group and the same solvent dose as the rapamycin group. For healthspan examination, the experiment commenced at 68 weeks of age, with samples collected at 84 weeks. For lifespan examination, mice were treated from age 70 weeks until death.

We also investigated whether DANA could counteract the side effects of E-motif in WT mice and those of human ELN fragments in immune-humanized mice. DANA (2.5 mg kg^{-1}) was intraperitoneally administered 10 min before each injection of 150 μg kg^{-1} E-motif or 500 μg kg^{-1} human ELN fragments through the tail vein (twice a week, 16-week treatment period, 32 total treatments). The treatment started at age 12 weeks in WT mice and 24 weeks in immune-humanized mice.

To investigate the roles of NEU1 in the E-motif-induced pro-aging effects of lymphocytes, we used two lymphocyte transplantation models. First, 12-week-old *Neu1*$^{-/-}$ donor mice were injected with or without 150 μg kg^{-1} E-motif through the tail vein (twice a week for 16 weeks, totaling 32 times). The two groups were named *Neu1*$^{-/-}$vehicle–T/B and *Neu1*$^{-/-}$E-motif–T/B. Sixteen weeks after the first injection, lymphocytes from donor mice were transplanted into *Rag1*$^{-/-}$ recipient mice, and the lifespan of the recipient mice was measured. The transplantation was performed twice at ages 30 and 50 weeks in *Rag1*$^{-/-}$ recipient mice. Second, 12-week-old WT donor mice were injected with or without 150 μg kg^{-1} E-motif through the tail vein and with or without 2.5 mg kg^{-1} DANA intraperitoneally 10 min before each E-motif application (twice a week for 16 weeks, totaling 32 times). The three groups were named T/B, E-motif–T/B and E-motif–DANA–T/B. Sixteen weeks after the first injection, lymphocytes from donor mice were transplanted into *Rag1*$^{-/-}$ recipient mice (described in 'Fluorescence-activated cell sorting and cell transplantation' in the Methods), and the lifespan of the recipient mice was measured. The transplantation was performed twice at ages 30 and 50 weeks in *Rag1*$^{-/-}$ recipient mice.

We also investigated whether DANA could counteract the side effects of E-motif in Yorkshire pigs (Jiagan Biotech). Following a concurrent quarantine and acclimatization period, pigs were maintained in a facility at 20–25 °C with a light–dark cycle and free access to food and water. DANA (2.5 mg kg^{-1}) was administered through the auricular vein 10 min before each injection of 150 μg kg^{-1} E-motif, also through the

auricular vein (twice a week over a 16-week treatment period, totaling 32 treatments). Sixteen weeks after the first injection, blood samples were collected from the pigs and analyzed. The experiments in pigs were started at age 24 weeks.

During all the above experiments, humane killing was performed by an experienced investigator or technician when the animals exhibited critical deterioration in mobility or developed severe pathological conditions associated with terminal morbidity, according to a previous study[65]. An animal was classified as severely moribund upon exhibiting more than one of the following clinical manifestations: (1) inability to eat or drink; (2) severe lethargy, as indicated by a lack of response, such as a reluctance to move when gently prodded with a pair of forceps; (3) severe balance or gait disturbance; (4) rapid weight loss over a period of 1 week or more; or (5) a severely ulcerated or bleeding tumor.

ELISA and blood biochemical testing

In Fig. 5l and Supplementary Fig. 7a, cytokines in mouse serum were assayed using a Luminex platform (Lx-MultiDTM-23, Shanghai Labex Biotech). In other experiments, cytokines and matrikines in mouse or human serum were analyzed using ELISA kits according to the manufacturer's instructions. The ELISA kits used for detecting matrikines were as follows: human ELN fragments (ml025439, Mlbio), mouse ELN fragments (ml057862, Mlbio), human COL fragments (type I COL, ml057441, Mlbio), mouse COL fragments (type I COL, ml002251, Mlbio), HA fragments (both human and mouse, DY3614, R&D Systems), human FN fragments (MK115, Takara) and mouse FN fragments (E04552m, Cusabio). During the detection of these matrikines in mice, we used the matrikines that were to be injected as standards. The ELISA kits used for detecting inflammatory factors and elastases included the following: IL-1 ELISA kit (JL20241, Shanghai Jianglai), MCP-1 ELISA kit (JL20304, Shanghai Jianglai), TNF ELISA kit (JL10484, Shanghai Jianglai), IL-6 ELISA kit (JL20268, Shanghai Jianglai), IFNγ ELISA kit (JL10967, Shanghai Jianglai), ME ELISA kit (EK0996, Boster) and NE ELISA kit (E-EL-M3025, Elabscience). The serum biochemical markers were detected by the Safety Assessment Center of Zhejiang University using an automatic biomedical analyzer (BS-240vet, Mindray).

Motor function and grasping ability measurements in mice

For treadmill running performance, mice were acclimated over 3 days at 5 m min^{-1} for 5 min, and mice that could not adapt were excluded from the analysis. A treadmill that delivers electric foot shocks (SA101C, Jiangsu Science Biological Technology) was used to stimulate the mice to run. On the test day, the initial speed was set at 1 m min^{-1}, with the acceleration set at 2 m min^{-2}. The number of electric shocks was recorded after 10 min or when the maximum number of 400 was reached.

Open field testing was performed in a 40 cm × 40 cm × 40.5 cm white box. Mice were allowed to familiarize themselves with the environment for 45 min before the experiment, and residual odors were removed with 75% alcohol. The mice were allowed to move spontaneously in a quiet environment, and parameters such as motion trajectory, total distance and mean speed were analyzed using ANY-maze software (Stoelting).

The hang wire test was conducted to assess forelimb muscle strength and grasping ability in mice. The apparatus consisted of a 5-mm-diameter metal rod suspended between two posts, 45 cm above a foam pillow. Before testing, each mouse underwent a 3-day acclimation period to familiarize itself with the apparatus. On the test day, each mouse was gently placed on the metal rod, allowing it to grasp the rod with its forelimbs. The time (in seconds) from placement on the rod until the mouse fell was recorded, with 120 s being the longest. Each mouse underwent three trials, with a 5-min rest period between trials. The average of the three trials was calculated.

Hematoxylin and eosin staining

Tissue specimens isolated from mice were fixed in 4% paraformaldehyde, washed overnight, dehydrated in graded ethanol, vitrified with dimethylbenzene, embedded in paraffin and cut into 5- to 7-μm sections. Paraffin sections hydrated with dimethylbenzene and graded ethanol were subjected to hematoxylin (03971, Sigma-Aldrich) and eosin (G1100, Solarbio) staining (H&E staining) for 5 min and 15 s, respectively. The sections were scanned using a digital scanner (VS200, Olympus), and images were analyzed using the corresponding xvViewer software for indicators including adipocyte area, muscle fiber cross-sectional area and epidermal thickness.

Determination of TG in liver tissue

Liver tissue was frozen in liquid nitrogen and ground in NP-40 lysate (P0013F, Beyotime). The homogenate was then heated to 80 °C to dissolve TG and centrifuged at 13,000*g* for 10 min. The supernatant was collected, and TG content was determined using a TG test kit (ab65336, Abcam) according to the manufacturer's instructions. The TG content was standardized by tissue weight.

Radiology assay

For micro-CT analysis, femur samples were scanned using a micro-CT scanner (U-CT-XUHR, MILabs) at a resolution of 4 μm. Three-dimensional structures were reconstructed with MILabs-Rec software. The analysis was performed on the 7-mm region starting from the distal femur using IMALYTICS Preclinical 2.1. software.

For the determination of the kyphosis index, X-ray images of the spinal column of mice were acquired using a mobile X-ray camera (XD56-5, Nanjing Perlove) at the Animal Hospital of Zhejiang University. The kyphosis index was calculated as described in a previous study[66]. Briefly, the kyphosis index was calculated as the distance from the caudal margin of the last cervical vertebra to the caudal margin of the sixth lumbar vertebra (usually corresponding to the cranial border of the wing of the ilium) divided by a perpendicular line running from the dorsal edge of the vertebra at the point of greatest curvature. Care was taken to avoid overextension or flexion of the limbs.

RNA extraction, sequencing and analysis

Tissues were ground, and total RNA was extracted using TRIzol reagent (9109, Invitrogen) according to the manufacturer's instructions. Then, 25–100 μl of DEPC-treated water was added to dissolve the RNA. Total RNA was qualified and quantified using a NanoDrop spectrophotometer and an Agilent 2100 bioanalyzer (NanoDrop One, Thermo Fisher Scientific).

For bulk RNA-seq, sequencing and library preparation were completed at the Beijing Genomics Institute (BGI). Briefly, purified mRNA was fragmented, followed by first-strand and second-strand cDNA synthesis. The cDNA fragments were amplified by PCR, and the PCR products were purified using AMPure XP beads to create DNA nanoballs, which had more than 300 copies of one molecule. The DNA nanoballs were loaded into the patterned nanoarray, and single-end 50 base reads were generated on the BGISEQ-500 platform (BGI-Shenzhen). Quality filtration was performed using SOAPnuke (v1.6.5)[67]. HISAT (v2.2.1) was used to map the reference genome[68]. The expression of each transcript was quantified using RSEM (v1.3.1)[69] and compared between groups using DESeq2, with a fold change of ≥2 and an adjusted *P* value (*Q* value) of ≤0.05. GO enrichment analysis was conducted using the TermFinder package, and KEGG (Kyoto Encyclopedia of Genes and Genomes) enrichment analysis was conducted using the phyper function in R software ($Q \leq 0.05$). GSEA was performed using GSEA 3.0 software, and normalized enrichment scores were used for plotting the GSEA-related heatmap.

For single-cell RNA-seq, sequencing was performed on the Illumina HiSeq X platform using the Singleron GEXSCOPE protocol for mRNA library construction. Raw data were processed by filtering read 1 for poly-T tails and extracting barcodes and unique molecular identifiers, along with trimming read 2 for adaptors and poly-A tails using fastp (v1.0)[70]. Reads were aligned to the Singleron Biotechnologies genome using STAR (v2.5.3a)[71], and gene expression was quantified

with featureCounts (v1.6.2)[72], yielding a matrix.tar archive containing barcodes.tsv, matrix.mtx and genes.tsv files. Downstream analysis was conducted in Seurat (v5.2.1)[73]. The expression matrix was loaded using Read10X, and cells with 200–6,000 RNA counts (nCount_RNA), 500–3,000 detected genes (nFeature_RNA) or >8% mitochondrial content (percent.mt), as well as genes present in fewer than three cells, were filtered. Data were normalized using SCTransform to identify variable genes[74]. The top 10 principal components from principal component analysis were used for clustering at a 0.5 resolution with the FindNeighbors and FindClusters functions. Clusters were annotated based on marker gene expression. Differential expression was analyzed using FindMarkers, and UMAP plots were generated with RunUMAP.

Quantitative real-time PCR

qPCR was conducted to evaluate the mRNA levels of genes. At the endpoint of each experiment, tissues were washed two times in PBS, added to TRIzol reagent and ground for RNA extraction. Reverse transcription was conducted using a commercial kit (R323, Vazyme) according to the manufacturer's instructions. The primers used for the qPCR analysis in this study are listed in Supplementary Table 3. qPCR reactions were performed using the TB Green PCR kit (Q711, Vazyme) according to the manufacturer's instructions.

Body composition analysis in mice

The mice were weighed, and the percentages of fat and lean tissues relative to body weight were measured using a low-field nuclear magnetic resonance body composition analyzer (QMR06-090H, Niumag).

Detection of luciferase activity

P16-3MR mice were treated with coelenterazine h (40906ES10, Yeasen Biotech) at a total dose of 20 mg kg^{-1} (10 mg kg^{-1} by tail vein injection and 10 mg kg^{-1} by dorsal subcutaneous injection) 10 min before imaging with an in vivo imaging system (IVIS Spectrum, Caliper).

Cytometry by time-of-flight

Blood was collected, and red blood cells were lysed using a lysis reagent (R1010, Solarbio). Antibody staining (Supplementary Table 4) and mass spectrometry were performed by PLT TECH in China. Data were preprocessed using FlowJo software, and cells were distinguished based on different markers using the PhenoGraph clustering algorithm[75]. The *t*-SNE dimensionality reduction algorithm was used to visualize cell clustering[76]. SPADE analysis was performed using Cytobank[77].

Markers of cell clusters were as follows: $CD4^+$ T cells ($B220^-$, $Gr1^-$, $CD3E^+$, $TCR\beta^+$, $CD4^+$, $CD8^-$), $CD8^+$ T cells ($B220^-$, $Gr1^-$, $CD3E^+$, $TCR\beta^+$, $CD4^-$, $CD8^+$), γδT cells ($B220^-$, $Gr1^-$, $CD3E^+$, $TCR\beta^-$, $TCR\gamma\delta^+$), natural killer cells ($NK1.1^+$, $CD3E^-$, $B220^-$, $CD19^-$), B cells ($CD3E^-$, $B220^+$, $CD19^+$), monocytes ($CD11B^+$, $LY6C^+$, $NK1.1^-$, $CD3E^-$, $CD19^-$, $B220^-$, $Fc\varepsilon RI\alpha^-$, $SiglecF^-$, $LY6G^-$), dendritic cells ($CD3E^-$, $B220^+$, $CD19^-$, $CD317^+$), neutrophils ($CD11B^+$, $LY6G^+$), eosinophilic granulocytes ($CD11B^+$, $SiglecF^+$) and basophilic granulocytes ($CD11B^+$, $Fc\varepsilon RI\alpha^+$, $SiglecF^-$, $LY6G^-$).

Flow cytometry

Blood or spleen samples were collected, and red blood cells were lysed. Cells were resuspended and stained with antibodies for 60 min on ice in the dark. Cells were washed and resuspended in PBS for flow cytometry analysis (CytoFLEX, Beckman). Cells were stained as follows: B cells ($CD45^+$, $CD19^+$), T cells ($CD45^+$, $CD3E^+$), neutrophils ($CD45^+$, $CD11B^+$, $LY6G^+$) and monocytes/macrophages ($CD45^+$, $CD11B^+$, $LY6G^-$, $CD3E^-$, $CD19^-$, $NK1.1^-$, $SiglecF^-$). Antibodies to the following proteins were used: CD45 (CD45-APC, eBioscience, 17-0454-811, 104, 1:50 dilution; CD45-FITC, BioLegend, 103107, 30-F11, 1:50 dilution), CD19 (CD19-APC/Cy7, BioLegend, 115529, 6D5, 1:50 dilution; CD19-PE, BioLegend, 115507, 6D5, 1:50 dilution), CD3E (CD3E-FITC, Invitrogen, 11-0031-82, 145-2C11, 1:50 dilution; CD3E-APC/Cy7, BioLegend, 100221, 17A2, 1:50 dilution), CD11B (CD11B-FITC, BioLegend, 101205, M1/70, 1:50 dilution), LY6G (LY6G-APC/Cy7, BioLegend, 127623, 1A8, 1:50 dilution; LY6G-APC, BioLegend, 127613, 1A8, 1:50 dilution), NK1.1 (NK1.1-APC, BioLegend, 156505, S17016D, 1:50 dilution; NK1.1-APC/Cy7, BioLegend, 108723, PK136, 1:50 dilution) and SiglecF (CD170-APC/Cy7, BioLegend, 155531, S17007L, 1:50 dilution).

Fluorescence-activated cell sorting and cell transplantation

Spleen lymphocytes ($CD45^+$, $CD3E^+$, $CD19^+$, $NK1.1^-$, $LY6G^-$, $LY6C^-$, $CD11B^-$), monocytes/macrophages ($CD45^+$, $CD11B^+$, $LY6G^-$, $CD3E^-$, $CD19^-$, $NK1.1^-$, $SiglecF^-$) and neutrophils ($CD45^+$, $CD11B^+$, $LY6G^+$) were sorted using a cell sorter (MoFlo Astrios EQ, Beckman). The antibodies used were the same as those in flow cytometry. Cells were washed and resuspended in DPBS for transplantation. Lymphocytes (2.5×10^6) or monocytes/macrophages (2.5×10^5) in 100 µl DPBS were transplanted into mice through tail vein injection.

To explore whether neutrophils and monocytes/macrophages mediate the E-motif-induced increases in the proportions of T/B cells, we administered 300 µg kg^{-1} E-motif to the donor mice. After 24 h, neutrophils or monocytes/macrophages were extracted, sorted and injected into the recipient mice. The injection was administered once a week for a total of five times. Samples were collected for analysis 1 week after the last injection.

Separation and treatment of mouse macrophages and neutrophils

Neutrophils were isolated from peripheral blood samples and collected in EDTA anticoagulant tubes using the EasySep mouse neutrophil enrichment kit (19762, STEMCELL Technologies). The isolated neutrophils were resuspended and cultured in RPMI 1640 medium (11875093, Gibco) containing 10% FBS. After 4 h of culture, the supernatant was collected, and the NE concentration was measured. The femurs and tibias were dissected from WT or LysM-Cre/*Neu1*-flox mice, and bone marrow was flushed with culture medium using a 1-ml syringe to acquire bone marrow-derived macrophages. Then, bone marrow-derived macrophages were cultured and purified in low-GLU DMEM (L-DMEM, C11885500BT, Gibco) containing 10% FBS and M-CSF (CB34, Novoprotein). After 24 h of culture, the supernatant was collected, and the ME concentration was measured. siRNA (5′ to 3′: *Neu1* sense, CAGGGAUAGUGUUCCUUAUTT; *Neu1* antisense, AUAAGGAACACUAUCCCUGTT; *Tlr4* sense, UUCUCCGAACGUGUCACGUTT; *Tlr4* antisense, ACGUGACACGUUCGGAGAATT; *Tlr2* sense, GGAACAGAGUGGCAACAGUTT; *Tlr2* antisense, ACUGUUGCCACUCUGUUCCTT) transfections were performed using Lipofectamine 2000 (11668019, Invitrogen) following the manufacturer's protocol. For the detection of the E-motif-induced inflammatory phenotype, the cells were treated with 2 µg ml^{-1} E-motif 36 h after transfections and left for 24 h. To determine whether DANA (GC44298, GlpBio) could alleviate the E-motif-induced secretion of inflammatory factors by macrophages in vitro, macrophages were isolated from WT mice. The cells were treated with 2 µg ml^{-1} E-motif alone or E-motif and 400 µmol l^{-1} DANA for 24 h. The culture supernatant was collected for ELISA.

Conditional gene knockout and cell deletion

LysM/iDTR mice express DTR mainly on myeloid cells[54,78]. To avoid the deletion of other important cells, we performed bone marrow transplantation as follows. WT mice were irradiated at a total dose of 10 Gy (two doses of 5 Gy each) using an X-ray bioirradiator (RS2000pro, Rad Source). After 3 h, 5×10^6 bone marrow cells from LysM/iDTR mice were transplanted into WT mice by tail vein administration to construct chimeric mice. After 3 months, E-motif and DT (15047A1, List Labs) were injected. DT was dissolved in PBS and administered intraperitoneally to chimeric mice. DT was administered 72, 48 and 24 h before the first E-motif injection at 20 µg kg^{-1} and 16 h before each subsequent E-motif injection at 5 µg kg^{-1}. To knock out the *Neu1* gene in LysM-Cre/*Neu1*-flox mice, tamoxifen (T5648, Sigma) was dissolved

in corn oil (C116023, Aladdin) and intraperitoneally injected at a dose of 100 mg kg^{-1} for five consecutive days before the E-motif treatment. E-motif administration began after the knockout of the gene was confirmed by western blot.

Western blot

RIPA lysis buffer (P0013B, Beyotime) containing protease and phosphatase inhibitors (78442, Thermo Fisher Scientific) was used for cell lysis, while the BCA assay (P0012S, Beyotime) was used for the quantification of protein concentrations. A 25 µg amount of total protein was loaded, and the gels were run for 1.5 h. The separated proteins were subsequently transferred to PVDF membranes (IPVH00010, Millipore). The membranes were blocked for 1 h and incubated with primary antibodies (NEU1, Santa Cruz, sc-166824, F-8, 1:1,000 dilution; tubulin, CST, 2144, 1:3,000 dilution) at 4 °C overnight. After incubating with secondary antibodies (anti-mouse HRP, Jackson ImmunoResearch, 115-035-003, 1:5,000 dilution; anti-rabbit HRP, ABclonal, AS014, 1:5,000 dilution) at room temperature for 1 h, the blot was imaged.

Clinical cohort study

Chronological age, sex, BMI, blood pressure, routine blood test results and blood biochemistry values were recorded. The following individuals were excluded: (1) pregnant women; (2) individuals with congenital or hereditary anemia, HIV, end-stage kidney disease, cirrhosis, blood cancer, bone marrow transplant and splenectomy, or other severe motor and/or mental disturbances; and (3) individuals whose predicted lifespan was less than 1 year. The superfluous blood samples were kept in a portable, insulated cool box with ice packs for up to a few hours before being taken to the local study laboratory for immediate processing. For serum acquisition, coagulated blood in ordinary tubes was centrifuged at 4 °C (1,500*g* for 5 min), and the supernatant was collected and stored at −80 °C for long-term preservation. This cohort included 1,068 eligible participants aged 20–96 years (male-to-female ratio, 553:515). The number of individuals in the different age groups was as follows: 20–30 years old, $n = 197$; 31–40 years old, $n = 233$; 41–50 years old, $n = 187$; 51–60 years old, $n = 187$; 61–70 years old, $n = 201$; >70 years old, $n = 63$.

To analyze the correlation between the serum content of ELN fragments and the physical examination index, ELN fragment contents were measured using ELISA (ml025439, Mlbio) in all samples. Linear regression was performed on ELN contents and various physical examination indices. The standardized β coefficient was used for plotting the heatmap. To explore whether there was a significant difference between the high ELN population and the normal ELN population, we defined the population with a serum content of ELN fragments of ≥1,500 pg ml^{-1} as the high ELN group (17.6%) and the population with 250 pg ml^{-1} ≤ ELN fragment content ≤ 680 pg ml^{-1} as the normal ELN group (37.5%). The physical examination indices of the two groups were compared. Figures 1a and 6e–h provide the results of the cohort studies.

Human monocytic THP-1 cells from ATCC were cultured with RPMI 1640 (11875093, Gibco) containing 10% FBS. THP-1 monocytes were differentiated into macrophages through a 24-h incubation with 150 nmol l^{-1} phorbol 12-myristate 13-acetate (P8139, Sigma). Age- and sex-matched human serum samples (from six male and six female participants in each group) from the high ELN group or the normal ELN group were added (10%, v/v) to the medium of human macrophages with or without 400 µmol l^{-1} DANA. When calculating the levels of inflammatory cytokines in the culture supernatant of treated macrophages, the amounts of the cytokines in the added human serum were subtracted.

Statistics and reproducibility

No statistical method was used to predetermine the sample size, but our sample sizes are similar to those reported in previous publications. The experiments were randomized, and the investigators were blinded to the group allocation during data collection, experimental procedures and analysis. Outliers were excluded from the analyses. Illustrations were created using FigDraw (https://www.figdraw.com) or are our original work.

All experimental groups included at least three biological replicates. Data are presented as mean ± s.d. (error bars represent s.d.). Measurements were obtained from independent samples collected from distinct mice. Statistical analyses and graph generation were performed using GraphPad Prism 8.0. Continuous variables were assumed to follow a normal distribution, although formal normality testing was not conducted. Pearson correlation coefficients with two-tailed 95% confidence intervals were used to assess correlations ($n \geq 30$). Survival analysis was performed using the log-rank (Mantel–Cox) test and the Gehan–Breslow–Wilcoxon test.

Two-way analysis of variance (ANOVA) was applied to analyze changes in body weight across multiple time points. For comparisons between two groups, either an unpaired two-tailed Student's *t* test (equal variance) or Welch's corrected unpaired *t* test (unequal variance) with a 95% confidence interval was used. One-way ANOVA followed by Tukey's post hoc test (for all pairwise comparisons) or Dunnett's test (for comparisons against a single control group) was used for multigroup analyses. Statistically significant *P* values were indicated as follows: no significance, $P \geq 0.05$; $^{*}P < 0.05$, $^{**}P < 0.01$, $^{***}P < 0.001$ and $^{****}P < 0.0001$.

Reporting summary

Further information on research design is available in the Nature Portfolio Reporting Summary linked to this article.

Data availability

The raw data from CyTOF in this study have been deposited in OMIX, China National Center for Bioinformation/Beijing Institute of Genomics, Chinese Academy of Sciences (accession no. OMIX006334). The raw RNA-seq data reported in this paper have been deposited in the Genome Sequence Archive of the National Genomics Data Center, China National Center for Bioinformation/Beijing Institute of Genomics, Chinese Academy of Sciences (GSA: CRA016019) and are publicly accessible at https://ngdc.cncb.ac.cn/gsa/browse/CRA016019. The raw data from single-cell RNA-seq have been deposited in the Genome Sequence Archive of the National Genomics Data Center, China National Center for Bioinformation/Beijing Institute of Genomics, Chinese Academy of Sciences (GSA: CRA025173) and are publicly accessible at https://ngdc.cncb.ac.cn/gsa/browse/CRA025173. All data in this article are provided in the source data files or available from the corresponding author upon reasonable request. Source data are provided with this paper.

References

1. Selman, M. & Pardo, A. Fibroageing: an ageing pathological feature driven by dysregulated extracellular matrix–cell mechanobiology. *Ageing Res. Rev.* **70**, 101393 (2021).
2. López-Otin, C., Blasco, M. A., Partridge, L., Serrano, M. & Kroemer, G. Hallmarks of aging: an expanding universe. *Cell* **186**, 243–278 (2023).
3. Smith, E. R. et al. Elastin degradation is associated with progressive aortic stiffening and all-cause mortality in predialysis chronic kidney disease. *Hypertension* **59**, 973–978 (2012).
4. Petersen, E., Wågberg, F. & Angquist, K.-A. Serum concentrations of elastin-derived peptides in patients with specific manifestations of atherosclerotic disease. *Eur. J. Vasc. Endovasc. Surg.* **24**, 440–444 (2002).
5. Skjøt-Arkil, H. et al. Measurement of MMP-9 and -12 degraded elastin (ELM) provides unique information on lung tissue degradation. *BMC Pulm. Med.* **12**, 34 (2012).

6. Kumavat, R. et al. Biomarkers of joint damage in osteoarthritis: current status and future directions. *Mediators Inflamm.* **2021**, 5574582 (2021).
7. Pérez-García, S. et al. Profile of matrix-remodeling proteinases in osteoarthritis: impact of fibronectin. *Cells* **9**, 40 (2019).
8. Wu, M. et al. A novel role of low molecular weight hyaluronan in breast cancer metastasis. *FASEB J.* **29**, 1290–1298 (2015).
9. Dominguez-Gutierrez, P. R. et al. Hyal2 expression in tumor-associated myeloid cells mediates cancer-related inflammation in bladder cancer. *Cancer Res.* **81**, 648–657 (2021).
10. Jariwala, N. et al. Matrikines as mediators of tissue remodelling. *Adv. Drug Deliv. Rev.* **185**, 114240 (2022).
11. Dokoshi, T. et al. Skin inflammation activates intestinal stromal fibroblasts and promotes colitis. *J. Clin. Invest.* **131**, e147614 (2021).
12. Feghali, K. & Grenier, D. Priming effect of fibronectin fragments on the macrophage inflammatory response: potential contribution to periodontitis. *Inflammation* **35**, 1696–1705 (2012).
13. Yi, J. et al. A pathological joint–liver axis mediated by matrikine-activated $CD4^+$ T cells. *Signal Transduct. Target. Ther.* **9**, 109 (2024).
14. Zhou, J.-S. et al. Cigarette smoke-initiated autoimmunity facilitates sensitisation to elastin-induced COPD-like pathologies in mice. *Eur. Respir. J.* **56**, 2000404 (2020).
15. Gayral, S. et al. Elastin-derived peptides potentiate atherosclerosis through the immune Neu1–PI3Kγ pathway. *Cardiovasc. Res.* **102**, 118–127 (2014).
16. Li, C.-J. et al. Senescent immune cells release grancalcin to promote skeletal aging. *Cell Metab.* **33**, 1957–1973 (2021).
17. Feng, X. et al. Senescent immune cells accumulation promotes brown adipose tissue dysfunction during aging. *Nat. Commun.* **14**, 3208 (2023).
18. Kawamoto, S. et al. Bacterial induction of B cell senescence promotes age-related changes in the gut microbiota. *Nat. Cell Biol.* **25**, 865–876 (2023).
19. Yousefzadeh, M. J. et al. An aged immune system drives senescence and ageing of solid organs. *Nature* **594**, 100–105 (2021).
20. Desdín-Micó, G. et al. T cells with dysfunctional mitochondria induce multimorbidity and premature senescence. *Science* **368**, 1371–1376 (2020).
21. Mitchell, C. A. et al. Stromal niche inflammation mediated by IL-1 signalling is a targetable driver of haematopoietic ageing. *Nat. Cell Biol.* **25**, 30–41 (2023).
22. Li, X. et al. Inflammation and aging: signaling pathways and intervention therapies. *Signal Transduct. Target. Ther.* **8**, 239 (2023).
23. Bonnans, C., Chou, J. & Werb, Z. Remodelling the extracellular matrix in development and disease. *Nat. Rev. Mol. Cell Biol.* **15**, 786–801 (2014).
24. Xu, M. et al. Senolytics improve physical function and increase lifespan in old age. *Nat. Med.* **24**, 1246–1256 (2018).
25. Maurice, P. et al. Elastin fragmentation and atherosclerosis progression: the elastokine concept. *Trends Cardiovasc. Med.* **23**, 211–221 (2013).
26. Tembely, D. et al. The elastin receptor complex: an emerging therapeutic target against age-related vascular diseases. *Front. Endocrinol. (Lausanne)* **13**, 815356 (2022).
27. Blanchevoye, C. et al. Interaction between the elastin peptide VGVAPG and human elastin binding protein. *J. Biol. Chem.* **288**, 1317–1328 (2013).
28. Heinz, A. et al. The action of neutrophil serine proteases on elastin and its precursor. *Biochimie* **94**, 192–202 (2012).
29. Jeon, O. H. et al. Local clearance of senescent cells attenuates the development of post-traumatic osteoarthritis and creates a pro-regenerative environment. *Nat. Med.* **23**, 775–781 (2017).
30. Furman, D. et al. Chronic inflammation in the etiology of disease across the life span. *Nat. Med.* **25**, 1822–1832 (2019).
31. Yu, L. et al. IgG is an aging factor that drives adipose tissue fibrosis and metabolic decline. *Cell Metab.* **36**, 793–807 (2024).
32. Mittelbrunn, M. & Kroemer, G. Hallmarks of T cell aging. *Nat. Immunol.* **22**, 687–698 (2021).
33. Sakata-Kaneko, S., Wakatsuki, Y., Matsunaga, Y., Usui, T. & Kita, T. Altered Th1/Th2 commitment in human $CD4^+$ T cells with ageing. *Clin. Exp. Immunol.* **120**, 267–273 (2000).
34. Kawai, T., Ikegawa, M., Ori, D. & Akira, S. Decoding Toll-like receptors: recent insights and perspectives in innate immunity. *Immunity* **57**, 649–673 (2024).
35. Chen, Q.-Q. et al. Neuraminidase 1 promotes renal fibrosis development in male mice. *Nat. Commun.* **14**, 1713 (2023).
36. Chen, Q.-Q. et al. Neuraminidase 1 is a driver of experimental cardiac hypertrophy. *Eur. Heart J.* **42**, 3770–3782 (2021).
37. Sieve, I. et al. A positive feedback loop between IL-1β, LPS and NEU1 may promote atherosclerosis by enhancing a pro-inflammatory state in monocytes and macrophages. *Vascul. Pharmacol.* **103–105**, 16–28 (2018).
38. Abdulkhalek, S. et al. Neu1 sialidase and matrix metalloproteinase-9 cross-talk is essential for Toll-like receptor activation and cellular signaling. *J. Biol. Chem.* **286**, 36532–36549 (2011).
39. Amith, S. R. et al. Neu1 desialylation of sialyl α-2,3-linked β-galactosyl residues of TOLL-like receptor 4 is essential for receptor activation and cellular signaling. *Cell. Signal.* **22**, 314–324 (2010).
40. Magesh, S., Suzuki, T., Miyagi, T., Ishida, H. & Kiso, M. Homology modeling of human sialidase enzymes NEU1, NEU3 and NEU4 based on the crystal structure of NEU2: hints for the design of selective NEU3 inhibitors. *J. Mol. Graph. Model.* **25**, 196–207 (2006).
41. Nikolov, A. et al. Abnormal levels of age-elastin derived peptides in sera of diabetic patients with arterial hypertension. *Cent. Eur. J. Immunol.* **39**, 345–351 (2014).
42. Romier, B. et al. Production of elastin-derived peptides contributes to the development of nonalcoholic steatohepatitis. *Diabetes* **67**, 1604–1615 (2018).
43. Blaise, S. et al. Elastin-derived peptides are new regulators of insulin resistance development in mice. *Diabetes* **62**, 3807–3816 (2013).
44. Robert, L. & Labat-Robert, J. Circulating elastin peptides, role in vascular pathology. *Pathol. Biol. (Paris)* **62**, 337–341 (2014).
45. Mogilenko, D. A. et al. Comprehensive profiling of an aging immune system reveals clonal $GZMK^+$ $CD8^+$ T cells as conserved hallmark of inflammaging. *Immunity* **54**, 99–115 (2021).
46. McLaughlin, T. et al. T-cell profile in adipose tissue is associated with insulin resistance and systemic inflammation in humans. *Arterioscler. Thromb. Vasc. Biol.* **34**, 2637–2643 (2014).
47. Senior, R. M., Griffin, G. L. & Mecham, R. P. Chemotactic activity of elastin-derived peptides. *J. Clin. Invest.* **66**, 859–862 (1980).
48. Lee, S.-H. et al. Antielastin autoimmunity in tobacco smoking-induced emphysema. *Nat. Med.* **13**, 567–569 (2007).
49. Gu, B.-H. et al. Elastin-specific autoimmunity in smokers with thoracic aortic aneurysm and dissection is independent of chronic obstructive pulmonary disease. *J. Am. Heart Assoc.* **8**, e011671 (2019).
50. Kawecki, C. et al. Identification of CD36 as a new interaction partner of membrane NEU1: potential implication in the pro-atherogenic effects of the elastin receptor complex. *Cell. Mol. Life Sci.* **76**, 791–807 (2019).
51. Guo, T. et al. Selective inhibitors of human neuraminidase 1 (NEU1). *J. Med. Chem.* **61**, 11261–11279 (2018).
52. Zhou, Z. et al. Type 2 cytokine signaling in macrophages protects from cellular senescence and organismal aging. *Immunity* **57**, 513–527 (2024).
53. Nguyen, T. T. & Corvera, S. Adipose tissue as a linchpin of organismal ageing. *Nat. Metab.* **6**, 793–807 (2024).
54. Wenzel, P. et al. Lysozyme M-positive monocytes mediate angiotensin II-induced arterial hypertension and vascular dysfunction. *Circulation* **124**, 1370–1381 (2011).

55. Guo, W., Zhang, C., Qiao, T., Zhao, J. & Shi, C. Strategies for the construction of mouse models with humanized immune system and evaluation of tumor immune checkpoint inhibitor therapy. *Front. Oncol.* **11**, 673199 (2021).
56. De La Rochere, P. et al. Humanized mice for the study of immuno-oncology. *Trends Immunol.* **39**, 748–763 (2018).
57. Pagano, M. & Reboud-Ravaux, M. Cryptic activities of fibronectin fragments, particularly cryptic proteases. *Front. Biosci. (Landmark Ed.)* **16**, 698–706 (2011).
58. Chubb, S. A. P. Measurement of C-terminal telopeptide of type I collagen (CTX) in serum. *Clin. Biochem.* **45**, 928–935 (2012).
59. Chen, L. et al. Association of osteoporosis and skeletal muscle loss with serum type I collagen carboxyl-terminal peptide β glypeptide: a cross-sectional study in elder Chinese population. *Open Med. (Wars.)* **18**, 20230642 (2023).
60. Zhuang, J. et al. Age-related accumulation of advanced oxidation protein products promotes osteoclastogenesis through disruption of redox homeostasis. *Cell Death Dis.* **12**, 1160 (2021).
61. Valicherla, G. R. et al. Evaluation of the pharmacokinetics of the pancreastatin inhibitor PSTi8 peptide in rats: integration of in vitro and in vivo findings. *Molecules* **27**, 339 (2022).
62. Aghazadeh-Habashi, A. & Khajehpour, S. Improved pharmacokinetics and bone tissue accumulation of Angiotensin-(1–7) peptide through bisphosphonate conjugation. *Amino Acids* **53**, 653–664 (2021).
63. Sumbria, R. K. et al. Pharmacokinetics and brain uptake of an IgG–TNF decoy receptor fusion protein following intravenous, intraperitoneal, and subcutaneous administration in mice. *Mol. Pharm.* **10**, 1425–1431 (2013).
64. Wrenn, D. S., Griffin, G. L., Senior, R. M. & Mecham, R. P. Characterization of biologically active domains on elastin: identification of a monoclonal antibody to a cell recognition site. *Biochemistry* **25**, 5172–5176 (1986).
65. Singh, P. et al. Taurine deficiency as a driver of aging. *Science* **380**, eabn9257 (2023).
66. Grunewald, M. et al. Counteracting age-related VEGF signaling insufficiency promotes healthy aging and extends life span. *Science* **373**, eabc8479 (2021).
67. Chen, Y. et al. SOAPnuke: a MapReduce acceleration-supported software for integrated quality control and preprocessing of high-throughput sequencing data. *Gigascience* **7**, 1–6 (2018).
68. Kim, D., Landmead, B. & Salzberg, S. L. HISAT: a fast spliced aligner with low memory requirements. *Nat. Methods* **12**, 357–360 (2015).
69. Li, B. & Dewey, C. N. RSEM: accurate transcript quantification from RNA-Seq data with or without a reference genome. *BMC Bioinformatics* **12**, 323 (2011).
70. Chen, S., Zhou, Y., Chen, Y. & Gu, J. fastp: an ultra-fast all-in-one FASTQ preprocessor. *Bioinformatics* **34**, i884–i890 (2018).
71. Dobin, A. et al. STAR: ultrafast universal RNA-seq aligner. *Bioinformatics* **29**, 15–21 (2013).
72. Liao, Y., Smyth, G. K. & Shi, W. featureCounts: an efficient general purpose program for assigning sequence reads to genomic features. *Bioinformatics* **30**, 923–930 (2014).
73. Hao, Y. et al. Dictionary learning for integrative, multimodal and scalable single-cell analysis. *Nat. Biotechnol.* **42**, 293–304 (2023).
74. Hafemeister, C. & Satija, R. Normalization and variance stabilization of single-cell RNA-seq data using regularized negative binomial regression. *Genome Biol.* **20**, 296 (2019).
75. Levine, J. H. et al. Data-driven phenotypic dissection of AML reveals progenitor-like cells that correlate with prognosis. *Cell* **162**, 184–197 (2015).
76. van der Maaten, L. & Hinton, G. Visualizing data using t-SNE. *J. Mach. Learn. Res.* **9**, 2579–2605 (2008).
77. Wu, H. et al. Single-cell mass cytometry reveals in vivo immunological response to surgical biomaterials. *Appl. Mater. Today* **16**, 169–178 (2019).
78. Miyake, Y. et al. Protective role of macrophages in noninflammatory lung injury caused by selective ablation of alveolar epithelial type II cells. *J. Immunol.* **178**, 5001–5009 (2007).

Acknowledgements

This work was supported by the National Key Research and Development Program of China (2022YFA1104600 to H.O. and X.Z.), the National Natural Sciences Foundation of China (T2121004, 82394441, 92268203 to H.O. and X.Z.) and the Key R&D Program of Zhejiang (2024SSYS0027 to H.O.). The funders had no role in study design, data collection and analysis, decision to publish or preparation of the manuscript.

Author contributions

J.Y.: conceptualization, methodology, investigation, formal analysis, writing—original draft, review and editing, creating figures; Y.W., H.S. and Z.C.: methodology, investigation, formal analysis, writing—original draft and editing, creating figures; B.W., J. Huang, J.W., W.S., P.J., X. Xia and X.Z.: resources; T.Y., T.T., F.B., X.C., Y.X., Y.Z., X. Xiao and J.Q.: methodology, investigation; X.Y., H.Z.: writing—editing; Y.C.: writing—editing; Z.Y.: resources, methodology; J. Hu and J.Z.: methodology; H.L.: methodology, project administration, conceptualization; H.O.: conceptualization, supervision, funding acquisition, project administration, writing—review and editing.

Competing interests

The authors declare no competing interests.

Additional information

Extended data is available for this paper at https://doi.org/10.1038/s43587-025-00961-8.

Supplementary information The online version contains supplementary material available at https://doi.org/10.1038/s43587-025-00961-8.

Correspondence and requests for materials should be addressed to Hongwei Ouyang.

Peer review information *Nature Aging* thanks Kyung A. Cho and the other, anonymous, reviewer(s) for their contribution to the peer review of this work.

https://doi.org/10.1038/s43587-025-00961-8

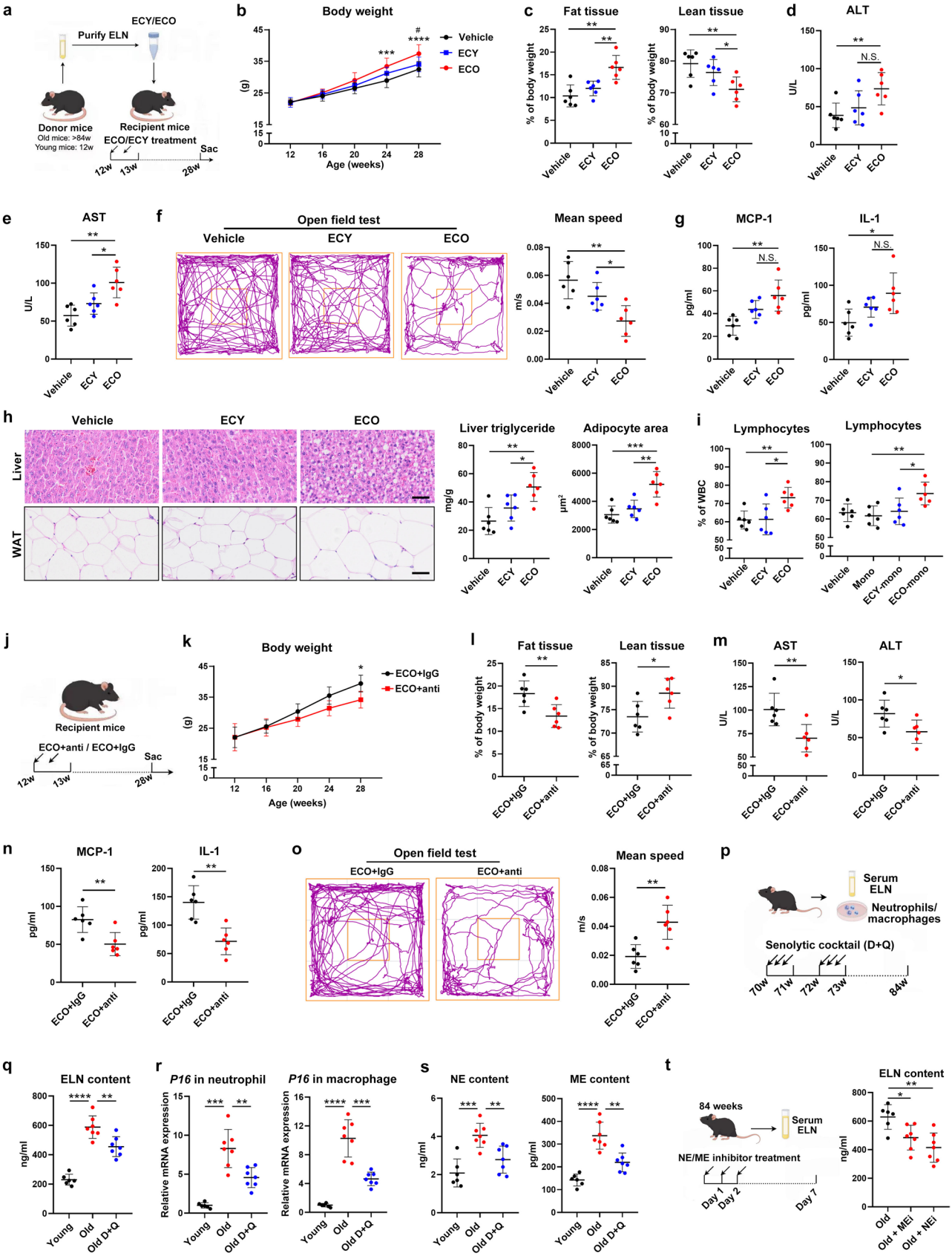

Extended Data Fig. 1 | See next page for caption.

https://doi.org/10.1038/s43587-025-00961-8

Extended Data Fig. 1 | Endogenous ELN fragments induce systemic aging in a positive feedback loop. a, Diagram illustrating the ELN fragments collected from old (ECO) or young (ECY) mice being injected into receptor young mice. **b**, Body weight changes of mice treated with ECO/ECY or vehicle over time (n = 6 per group, ECO versus vehicle at 24 weeks $P = 0.0003$, at 28 weeks $P < 0.0001$). **c**, The proportion of fat tissue (left) or lean tissue (right) to the total body weight in mice at the experimental endpoint (n = 6 per group, Fat tissue: ECO versus vehicle $P = 0.0016$, ECO versus ECY $P = 0.0044$; Lean tissue: ECO versus vehicle $P = 0.0066$, ECO versus ECY $P = 0.0443$). **d**,**e**, Serum levels of ALT and AST (n = 6 per group, ALT: ECO versus vehicle $P = 0.0091$; AST tissue: ECO versus vehicle $P = 0.0014$, ECO versus ECY $P = 0.0194$). **f**, Open field test, including movement trajectories (left) and average speed (right) (n = 6 per group, ECO versus vehicle $P = 0.0020$, ECO versus ECY $P = 0.0151$). **g**, Serum levels of MCP-1 and IL-1 (n = 6 per group, MCP-1: ECO versus vehicle $P = 0.0022$; IL-1: ECO versus vehicle $P = 0.0147$). **h**, Representative H&E-stained images of liver and white adipose tissue (WAT), with corresponding quantification of hepatic triglyceride content and adipocyte area. (n = 6 per group, Liver triglyceride: ECO versus vehicle $P = 0.0018$, ECO versus ECY $P = 0.0243$; Adipocyte area: ECO versus vehicle $P = 0.0007$, ECO versus ECY $P = 0.0030$). Scale bar = 50 μm. **i**, The proportion of lymphocyte in WBC after direct injection of ECO/ECY (left) or injection with monocytes/macrophages sorted from ECO/ECY-treated mice (n = 6 per group, Lymphocytes: ECO versus vehicle $P = 0.0025$, ECO versus ECY $P = 0.0166$; Lymphocytes: ECO-mono versus Mono $P = 0.0045$, ECO-mono versus ECY-mono $P = 0.0312$). **j**, Diagram illustrating ECO treatment in combination with IgG or anti-elastin antibody. **k**, Body weight changes of mice treated with ECO+IgG or ECO+antibody over time (n = 6 per group, ECO+antibody versus ECO+IgG $P = 0.0137$ at 28 weeks). **l**, The proportion of fat tissue (left) or lean tissue (right) to the total body weight in mice at the experimental endpoint (n = 6 per group, Fat tissue: ECO+anti versus ECO+IgG $P = 0.0094$; Lean tissue: ECO+anti versus ECO+IgG $P = 0.0224$). **m**, Serum levels of AST and ALT (n = 6 per group, AST: ECO+anti versus ECO+IgG $P = 0.0081$; ALT: ECO+anti versus ECO+IgG $P = 0.0319$). **n**, Serum levels of MCP-1 and IL-1 (n = 6 per group, MCP-1: ECO+anti versus ECO+IgG $P = 0.0060$; IL-1: ECO+anti versus ECO+IgG $P = 0.0012$). **o**, Open field test, including movement trajectories and average speed (n = 6 per group, ECO+anti versus ECO+IgG $P = 0.0024$). **p**, Diagram illustrating senolytic cocktail treatment regimen and subsequent examination. **q**, Serum levels of ELN fragments (Young group: n = 6, Old and Old D + Q groups: n = 7; Old versus Young $P < 0.0001$, Old D + Q versus Old $P = 0.0048$). **r**, qPCR analysis of $P16^{INK4A}$ in neutrophils (left) and macrophages (right) (Young group: n = 6, Old and Old+Q groups: n = 7; P16 in neutrophil: Old versus Young $P = 0.0002$, Old D + Q versus Old $P = 0.0038$; P16 in macrophage: Old versus Young $P < 0.0001$, Old D + Q versus Old $P = 0.0008$). **s**, Levels of neutrophil elastase (NE) (left) and macrophage elastase (ME) (right) in the supernatant of cultured neutrophils and macrophages, respectively (Young group: n = 6, Old and Old+Q groups: n = 7; NE content: Old versus Young $P = 0.0003$, Old D + Q versus Old $P = 0.0039$; ME content: Old versus Young $P < 0.0001$, Old D + Q versus Old $P = 0.0010$). **t**, Diagram illustrating NE inhibitor or ME inhibitor treatment regimen and subsequent examination (left). Serum levels of ELN fragments (right) (Young group: n = 6, Old and Old+Q groups: n = 7; Old versus Old+MEi $P = 0.0117$, Old+MEi versus Old+NEi $P = 0.0019$). * $P < 0.05$, ** $P < 0.01$, *** $P < 0.001$, **** $P < 0.0001$, $^{\#}P < 0.05$. Scale bar = 50 μm for **h**. Two-way ANOVA (**b**,**k**). Unpaired two-tailed Student's t-test (equal variance) or unpaired two-tailed with Welch's correction (unequal variance) with a 95% confidence interval (**c**-**i**,**l**-**o**,**q**-**t**). Data are presented as mean values ± SD. Illustrations in panels **a**, **j**, **p**, **t** were created using FigDraw.

https://doi.org/10.1038/s43587-025-00961-8

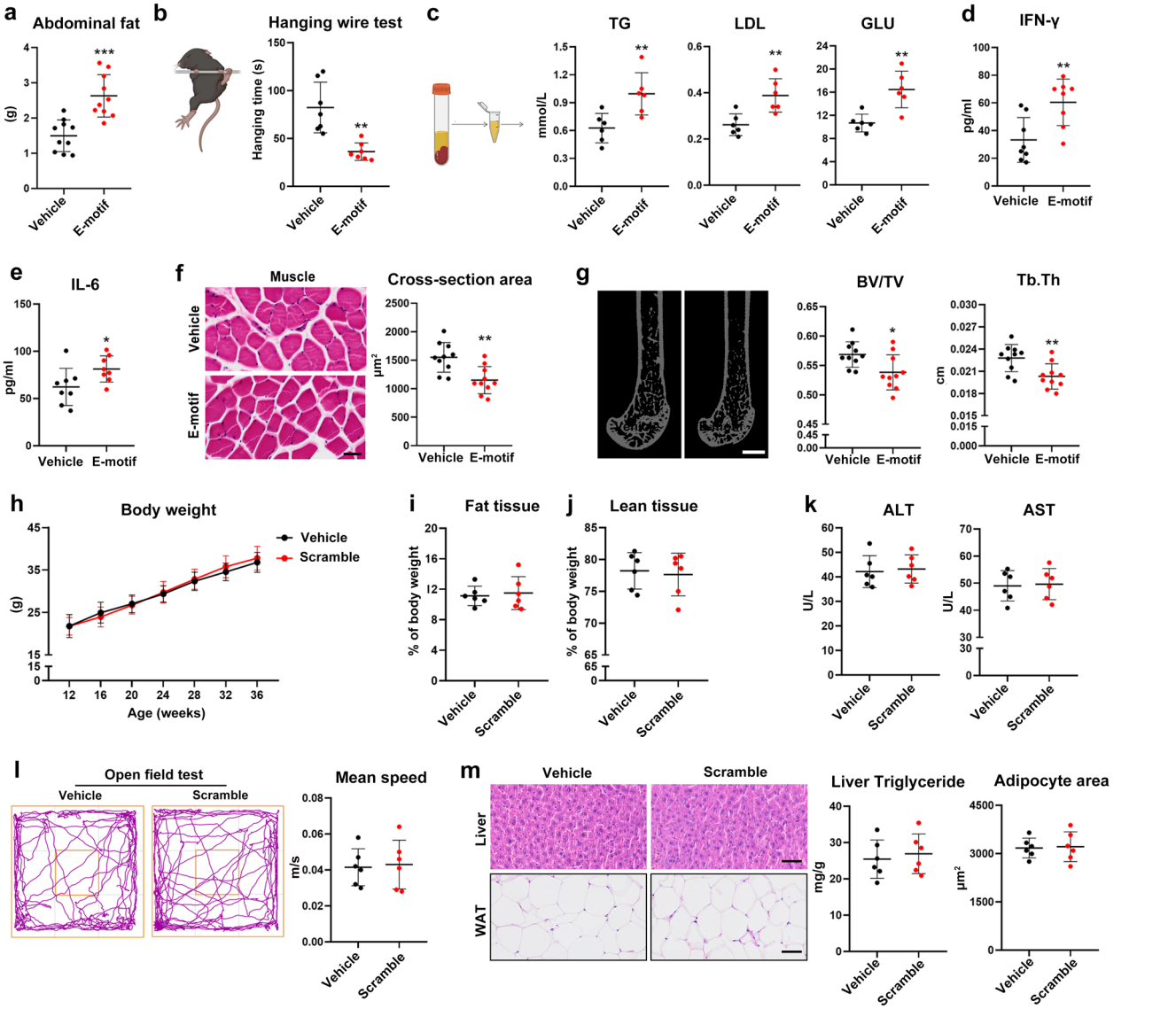

Extended Data Fig. 2 | E-motif induces systemic aging. a, The weight of abdominal fat of mice at the experimental endpoint **a**ged 36 weeks) (n = 10 per group, E-motif versus vehicle $P = 0.0002$). **b**, Hang wire test and corresponding quantification of hanging time (n = 7 per group, E-motif versus vehicle $P = 0.0029$). Illustration was created using FigDraw. **c**, Serum biochemistry analysis (TG, LDL, and GLU levels) in mice (n = 6 per group, TG: E-motif versus vehicle $P = 0.0086$; LDL: E-motif versus vehicle $P = 0.0049$; GLU: E-motif versus vehicle $P = 0.0024$). **d,e**, Levels of serum inflammatory markers (IFN-γ and IL-6) in mice (n = 8 per group, IFN-γ: E-motif versus vehicle $P = 0.0053$; IL-6: E-motif versus vehicle $P = 0.0415$). **f**, Representative H&E-stained images of muscle fibers (left) and quantification of cross-sectional areas (right) (n = 10 per group, scale bar = 50 μm, E-motif versus vehicle $P = 0.0021$). **g**, Representative micro-CT images of bone tissue and the quantification of bone volume/tissue volume (BV/TV) and trabecular thickness (Tb.Th) (n = 10 per group, scale bar = 1 mm, BV/TV: E-motif versus vehicle $P = 0.0183$; Tb.Th: E-motif versus vehicle $P = 0.0059$). **h**, Body weight changes of mice treatment with scramble peptide or vehicle over time (n = 6 per group). **i,j**, The proportion of fat tissue (**i**) or lean tissue (**j**) to the total body weight in mice at the experimental endpoint (n = 6 per group). **k**, Serum levels of ALT and AST (n = 6 per group). **l**, Open field test, including movement trajectories and average speed (n = 6 per group). **m**, Representative H&E-stained images of liver tissue and WAT and the quantification of triglyceride content and adipocyte areas (n = 6 per group). All the comparison between Scramble and vehicle group did not show statistical significance. * $P < 0.05$, ** $P < 0.01$, *** $P < 0.001$, **** $P < 0.0001$. Scale bar = 1 mm for **g** and scale bar = 50 μm for **f**,**m**. Two-way ANOVA (**h**). Unpaired two-tailed Student's t-test (equal variance) or unpaired two-tailed with Welch's correction (unequal variance) with a 95% confidence interval (**a**-**g**,**i**-**m**). Data are presented as mean values ± SD.

https://doi.org/10.1038/s43587-025-00961-8

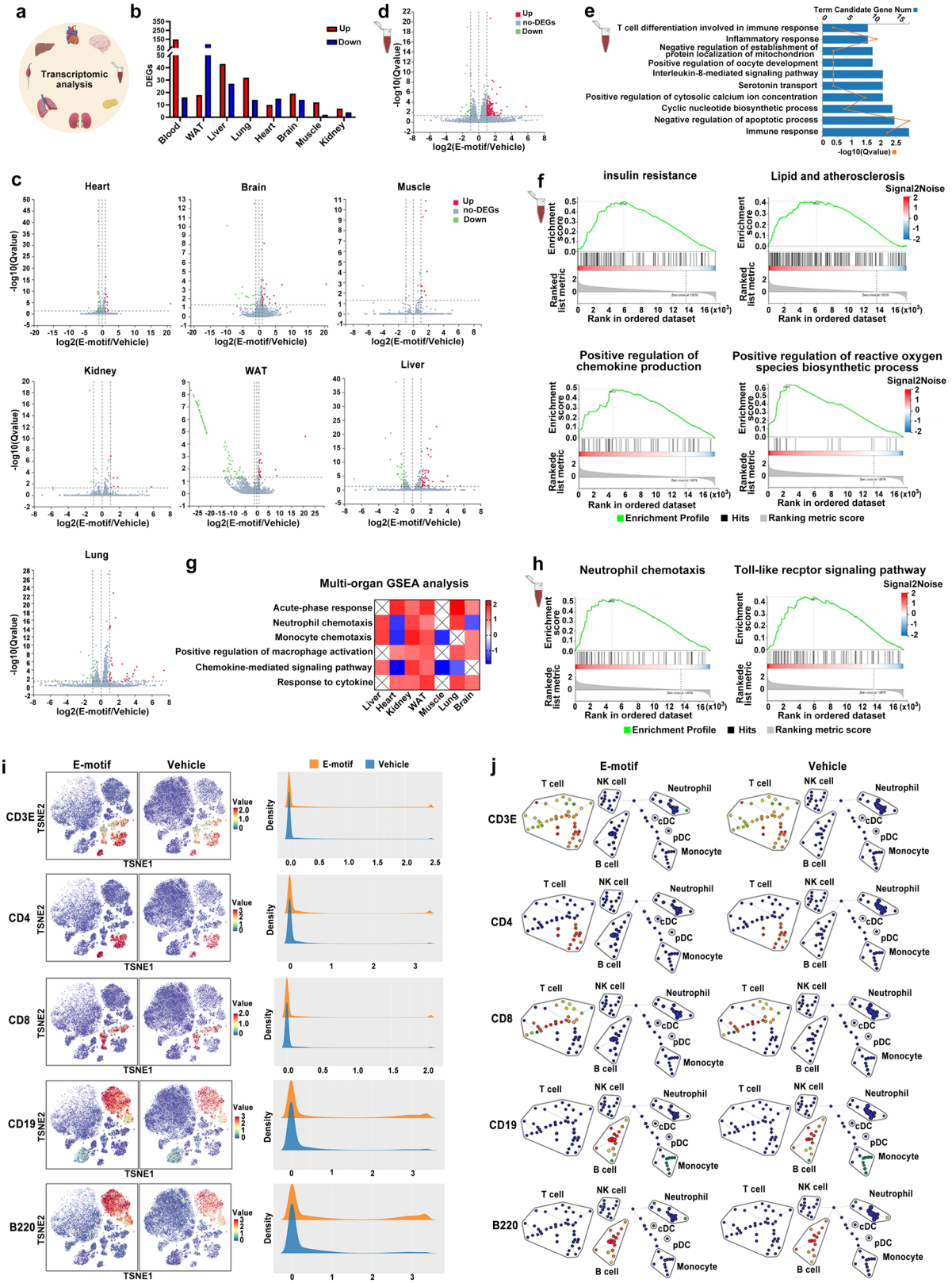

Extended Data Fig. 3 | See next page for caption.

https://doi.org/10.1038/s43587-025-00961-8

Extended Data Fig. 3 | Multi-omic analysis of E-motif treated mice. a,**b**, Schematic representation of RNAseq of multi-tissue including heart, liver, muscle, lung, kidney, WAT, PBMCs and brain (**a**) and quantification of differential expressed genes (DEGs) (**b**) (n = 3 per group). Red bar showed the number of upregulated DEGs in E-motif group. Illustration in panel **a** was created using FigDraw. **c**, Volcano plots displaying DEGs across heart, liver, muscle, lung, kidney, WAT and brain tissues (n = 3 per group). **d**, Volcano plot displaying DEGs in PBMCs between the E-motif and the vehicle group (n = 3 per group). **e**, Top10 terms upregulated in the E-motif group based on GO enrichment analysis of PBMCs transcriptomic data (n = 3 per group). **f**, GSEA analysis identifying pathways upregulated in the E-motif group in PBMCs (n = 3 per group). **g**, GSEA analysis across multiple solid organs with normalized enrichment score (NES) values represented in a heatmap. Red block means upregulation in the E-motif group (n = 3 per group). **h**, GSEA analysis identifying pathways upregulated in the E-motif group in PBMCs (n = 3 per group). **i**, T-SNE dimensionality reduction plot (left) and histogram plot (right) showing relative expression of protein markers (n = 5 per group). **j**, SPADE tree derived from CyTOF data illustrating relationships between cell clusters and relative expression of protein markers (n = 5 per group).

https://doi.org/10.1038/s43587-025-00961-8

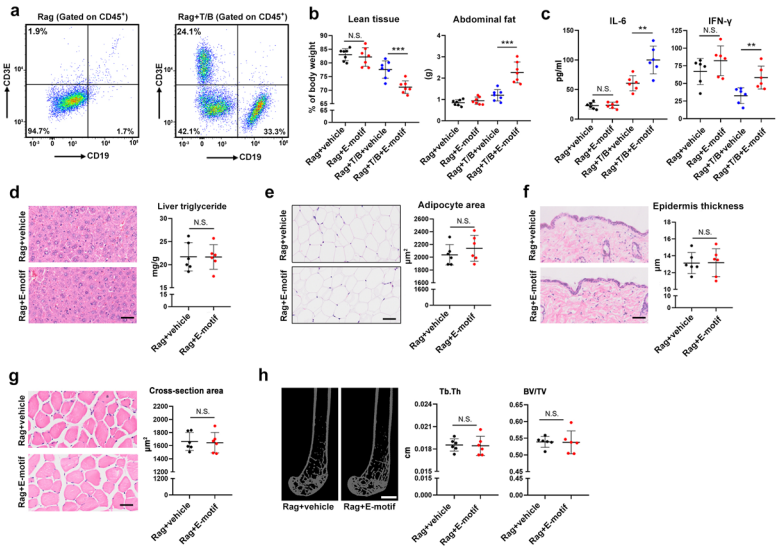

Extended Data Fig. 4 | Lymphocyte activation mediated E-motif induced systemic aging. a, Flow cytometry analysis of Rag mice (left) and Rag mice adoptively transferred with T/B cells (right). **b**, The proportion of lean tissue to total body weight (left) and the weight of abdominal fat in mice at the experimental endpoint (n = 7 per group, Lean tissue: Rag+T/B + E-motif versus Rag+T/B+vehicle $P = 0.0010$; Abdominal fat: Rag+T/B + E-motif versus Rag+T/B+vehicle $P = 0.0003$). **c**, Serum levels of IL-6 and IFN-γ (n = 6 per group, IL-6: Rag+T/B + E-motif versus Rag+T/B+vehicle $P = 0.0047$; IFN-γ: Rag+T/B + E-motif versus Rag+T/B+vehicle $P = 0.0095$). **d**, Representative H&E-stained images of liver tissue (left) and the quantification of triglyceride content (right) (n = 6 per group). **e**, Representative H&E-stained images of WAT (left) and the quantification of adipocyte areas (right) (n = 6 per group). **f**, Representative H&E-stained images of skin tissue (left) and the quantification of epidermal thickness (right). **g**, Representative H&E-stained images of muscle fibers (left) and the quantification of cross-sectional areas (right) (n = 6 per group). **h**, Representative micro-CT images of bone tissue and the quantification of BV/TV and Tb.Th (n = 6 per group). ** $P < 0.01$, *** $P < 0.001$. Scale bar = 1 mm for **h**, scale bar = 50 μm for **d**-**g**. Unpaired two-tailed Student's t-test with a 95% confidence interval (**b**-**h**).

https://doi.org/10.1038/s43587-025-00961-8

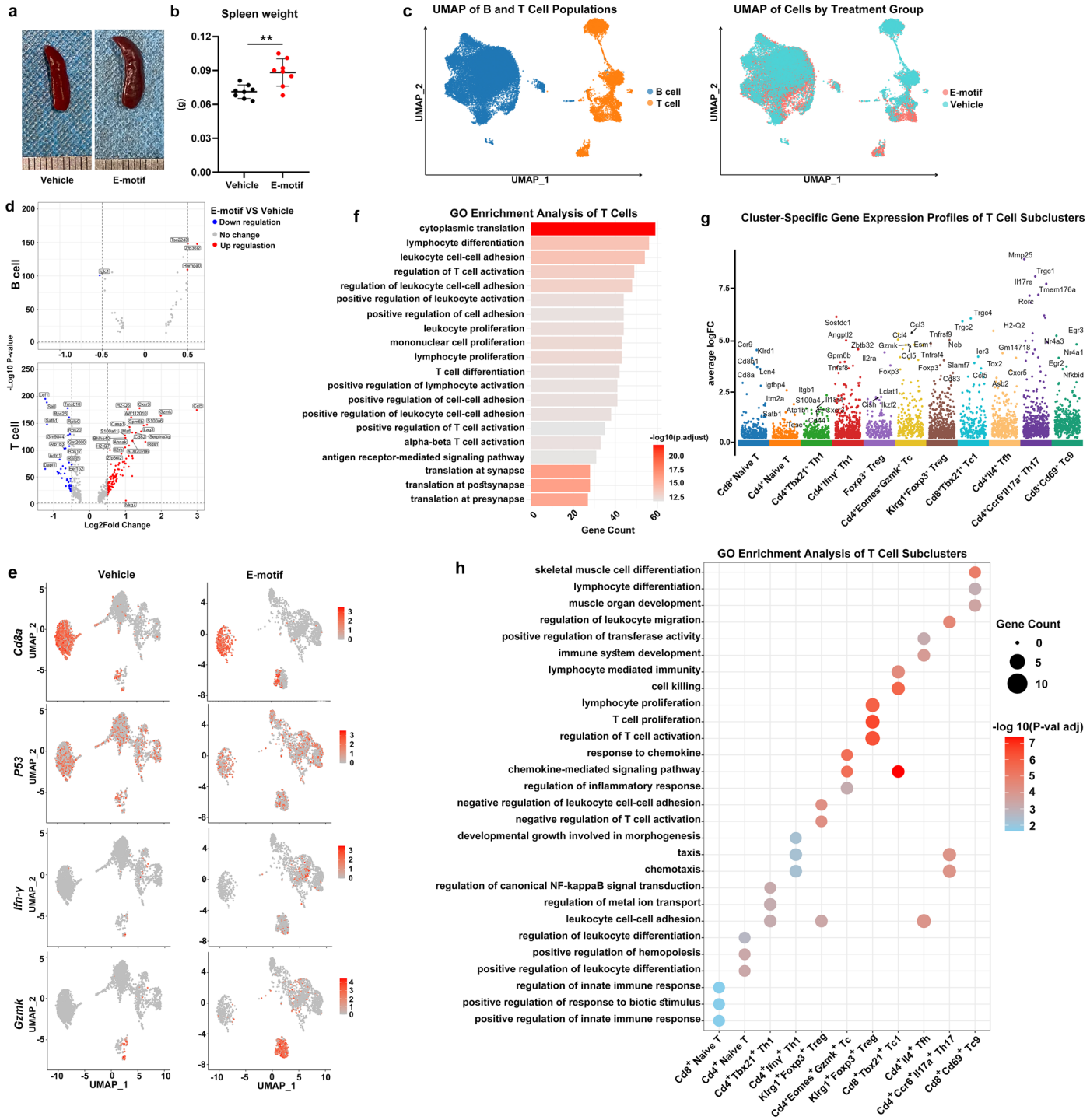

Extended Data Fig. 5 | Single-cell transcriptomic analysis of splenic lymphocyte after long-term E-motif treatment. a,**b**, Plot of spleen (**a**) and the quantification of spleen weight (**b**) (n = 8 per group, Spleen weight: E-motif versus vehicle $P = 0.0032$). **c**, UMAP plots of all the cells colored by cell type (T cells vs. B cells, left) and by treatment group (E-motif vs. vehicle, right). **d**, Volcano plots showing differentially expressed genes (DEGs) between vehicle and E-motif groups for T cells and B cells, respectively. **e**, UMAP feature plots showing increased expression of aging-associated genes (*Cd8a*, *P53*, *Ifn-γ* and *Gzmk*) in E-motif-treated cells. **f**, Top20 terms of GO enrichment analysis (Biological Process) of DEGs upregulated in E-motif group. **g**, Cluster-specific gene expression profiles of T cell subtypes, highlighting distinct transcriptional signatures across subsets. **h**, GO enrichment analysis (Biological Process) of individual T cell subclusters upregulated by E-motif treatment. $^{**}P < 0.01$. In each group of single-cell RNAseq, 6 mice were pooled together for detection. Unpaired two-tailed Student's *t*-test with a 95% confidence interval (**b**).

https://doi.org/10.1038/s43587-025-00961-8

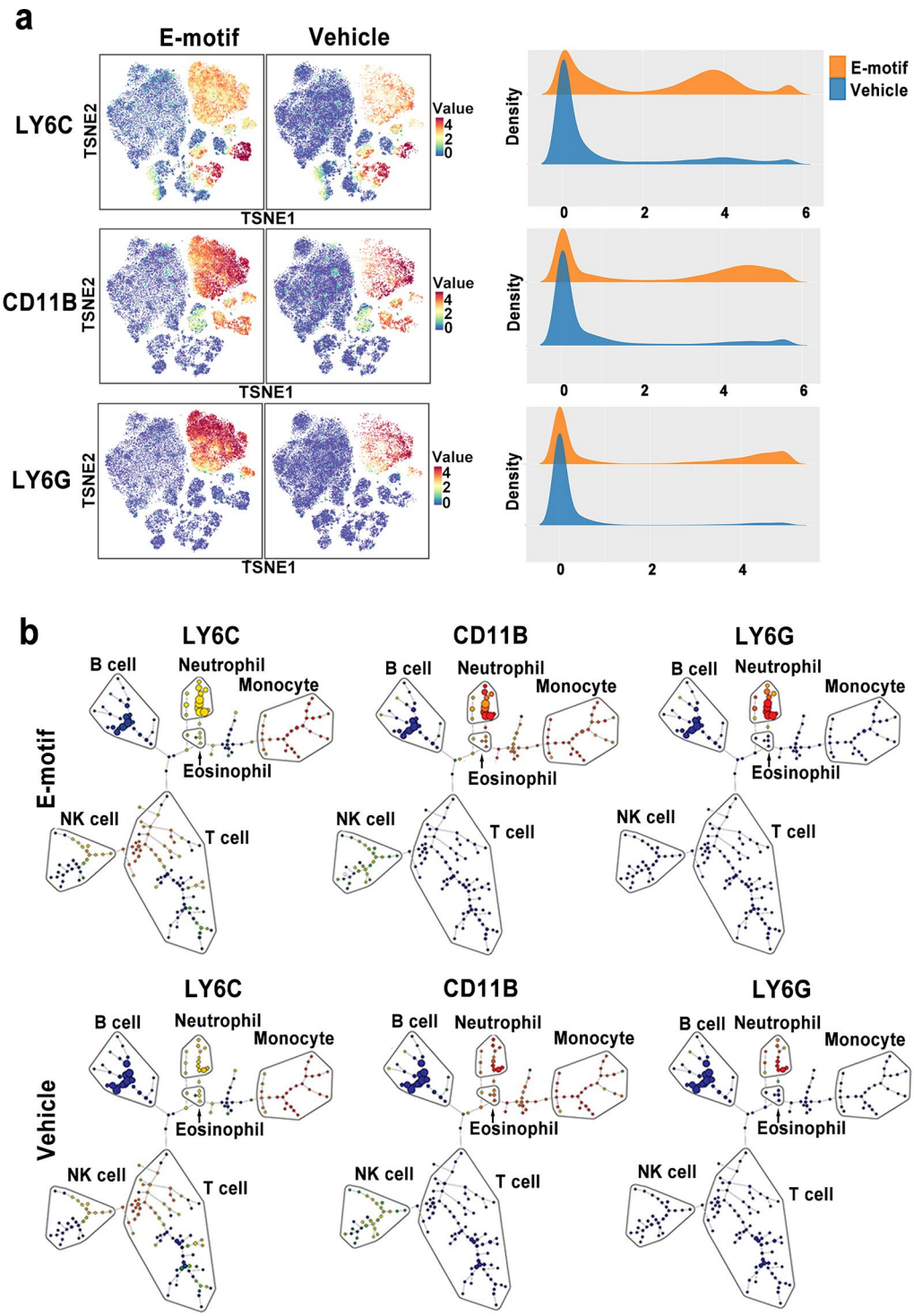

Extended Data Fig. 6 | Cytof analysis of PBMCs after 24-hour E-motif treatment. a, T-SNE dimensionality reduction plot and histogram plot illustrating relative expression of protein markers (n = 5 per group). **b**, SPADE tree derived from CyTOF data, illustrating relationships between cell clusters and relative expression of protein markers (n = 5 per group).

https://doi.org/10.1038/s43587-025-00961-8

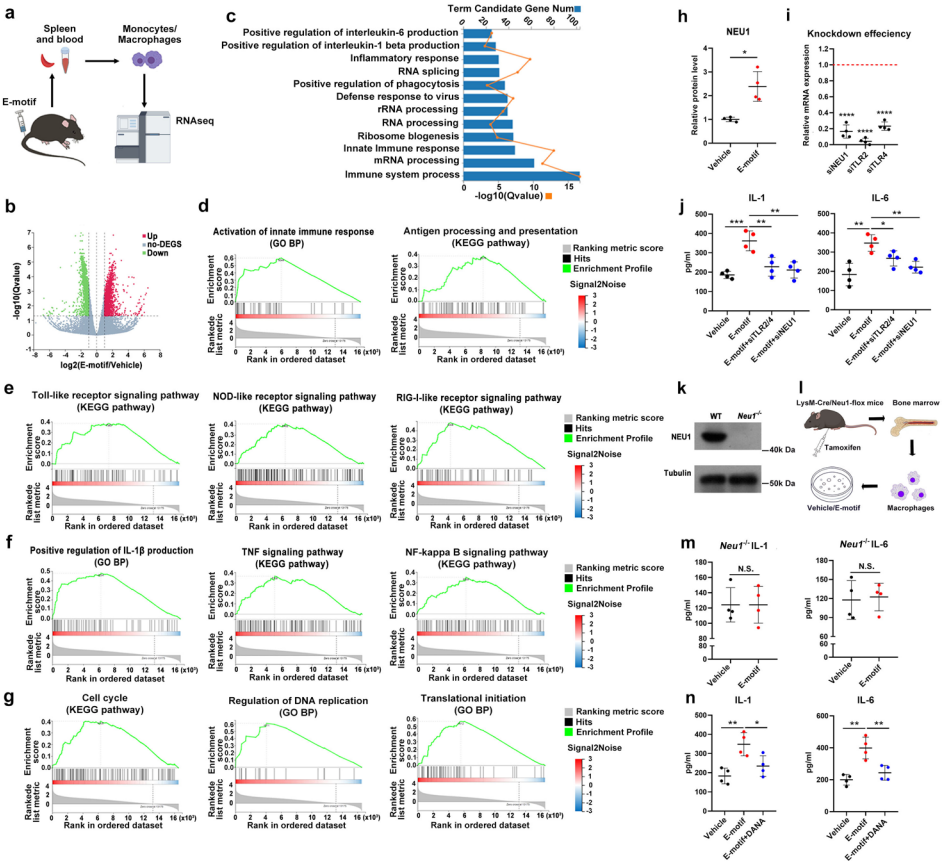

Extended Data Fig. 7 | E-motif induces inflammation in myeloid cells through NEU1. a, Schematic representation of spleen and blood extraction and monocytes/macrophages sorting after E-motif injection. **b**, Volcano plot illustrating differential gene expression between the E-motif and vehicle groups (n = 3 per group). **c**, GO enrichment analysis depicting the top12 upregulated terms in monocytes/macrophages in the E-motif group (n = 3 per group). **d - g** GSEA analysis of genes upregulated by E-motif in the "GO Biological Process" and "KEGG pathway" dataset (n = 3 per group). **h**, Quantitative analysis of western blot in Fig. 4i (n = 4 per group, E-motif versus vehicle $P = 0.0202$). **i**, qPCR analysis of *Neu1*, *Tlr-2* and *Tlr-4* gene expression to verify the knockdown efficiency of siRNA (n = 4 per group, $P < 0.0001$ for all groups). The red dashed line indicates relative gene expression in the vehicle group. **j**, IL-1 and IL-6 levels in cultural supernatant of bone marrow-derived macrophages from wild-type mice (n = 4 per group, IL-1: E-motif versus vehicle $P = 0.0007$, E-motif versus E-motif+siTLR2/4 $P = 0.0092$, E-motif versus E-motif+siNEU1 $P = 0.0039$; IL-6: E-motif versus vehicle $P = 0.0040$, E-motif versus E-motif+siTLR2/4 $P = 0.0342$, E-motif versus E-motif+siNEU1 $P = 0.0031$). **k**, Western blot analysis of NEU1 protein level in $Neu1^{f/f}$ (without tamoxifen treatment) and $Neu1^{-/-}$ mice. **l**, Illustrative representation of the process of obtaining macrophages from the bone marrow of $Neu1^{-/-}$ mice. **m**, IL-1 and IL-6 levels in cultural supernatant of bone marrow-derived macrophages from $Neu1^{-/-}$ mice after E-motif treatment. **n**, IL-1 and IL-6 levels in cultural supernatant of bone marrow-derived macrophages from wild-type mice after E-motif or E-motif+DANA treatment (n = 4 per group, IL-1: E-motif versus vehicle $P = 0.0039$, E-motif+DANA versus E-motif $P = 0.0305$; IL-6: E-motif versus vehicle $P = 0.0019$, E-motif+DANA versus E-motif $P = 0.0093$). * $P < 0.05$, ** $P < 0.01$, *** $P < 0.001$. Unpaired two-tailed Student's t-test (equal variance) or unpaired two-tailed with Welch's correction (unequal variance) with a 95% confidence interval (**h-j**,**m**,**n**). Illustrations in panels **a** and **l** were created using FigDraw.

https://doi.org/10.1038/s43587-025-00961-8

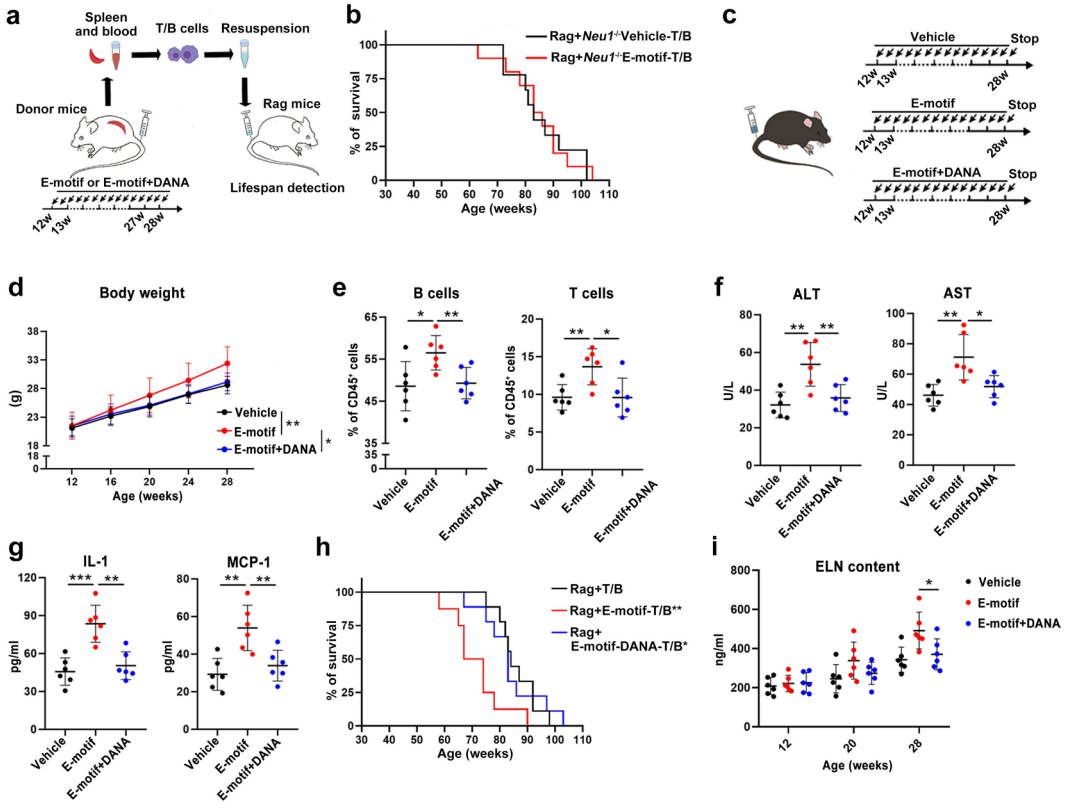

Extended Data Fig. 8 | DANA counteract E-motif-induced systemic aging. **a**, Diagram illustrating cell transplantation using mice injected with E-motif or E-motif+DANA as donors. **b**, Survival curves for Rag mice after adoptively transferred with T/B cells from *Neu1*$^{-/-}$ mice treated with or without E-motif (Rag+*Neu1*$^{-/-}$vehicle-T/B: n = 9, Rag+*Neu1*$^{-/-}$E-motif-T/B: n = 10, no significant difference between Rag+*Neu1*$^{-/-}$E-motif-T/B and Rag+*Neu1*$^{-/-}$vehicle-T/B). **c**, Illustrative representation of three groups of different treatment (vehicle, E-motif, and E-motif combined with DANA) over a 16-week period to verify the roles of DANA. Illustration was created using FigDraw. **d**, Body weight changes of mice treatment with E-motif, E-motif+DANA or vehicle over time (n = 6 per group; E-motif versus vehicle $P = 0.0079$, E-motif+DANA versus E-motif $P = 0.0297$). **e**, The ratio of T/B cells in peripheral blood (n = 6 per group, B cells: E-motif versus vehicle $P = 0.0218$, E-motif+DANA versus E-motif $P = 0.0097$; T cells: E-motif versus vehicle $P = 0.0069$, E-motif+DANA versus E-motif $P = 0.0173$). **f**,**g**, Serum levels of ALT, AST, IL-1 and MCP-1 (n = 6 per group, ALT: E-motif versus vehicle $P = 0.0028$, E-motif+DANA versus E-motif $P = 0.0092$; AST: E-motif versus vehicle $P = 0.0040$, E-motif+DANA versus E-motif $P = 0.0170$; IL-1: E-motif versus vehicle $P = 0.0005$, E-motif+DANA versus E-motif $P = 0.0013$; MCP-1: E-motif versus vehicle $P = 0.0022$, E-motif+DANA versus E-motif $P = 0.0072$). **h**, Survival curves for mice after cell transplantation using mice injected with E-motif or E-motif+DANA as donors (Rag-T/B and Rag+E-motif-DANA-T/B: n = 9 per group, Rag+E-motif-T/B: n = 8; Rag+E-motif-T/B versus Rag-T/B $P = 0.0061$ by log-rank test and $P = 0.0025$ by Gehan–Breslow–Wilcoxon test, Rag+E-motif-T/B versus Rag+E-motif-DANA-T/B $P = 0.0279$ by log-rank test and $P = 0.0172$ by Gehan–Breslow–Wilcoxon test). **i**, Serum levels of ELN fragments (n = 6, E-motif+DANA versus E-motif $P = 0.0364$). * $P < 0.05$, ** $P < 0.01$, *** $P < 0.001$. Unpaired two-tailed Student's t-test with a two-tailed 95% confidence interval (**e**-**g**). Log-rank test and Gehan–Breslow–Wilcoxon test (**b**,**h**). Two-way ANOVA (**d**,**i**).

https://doi.org/10.1038/s43587-025-00961-8

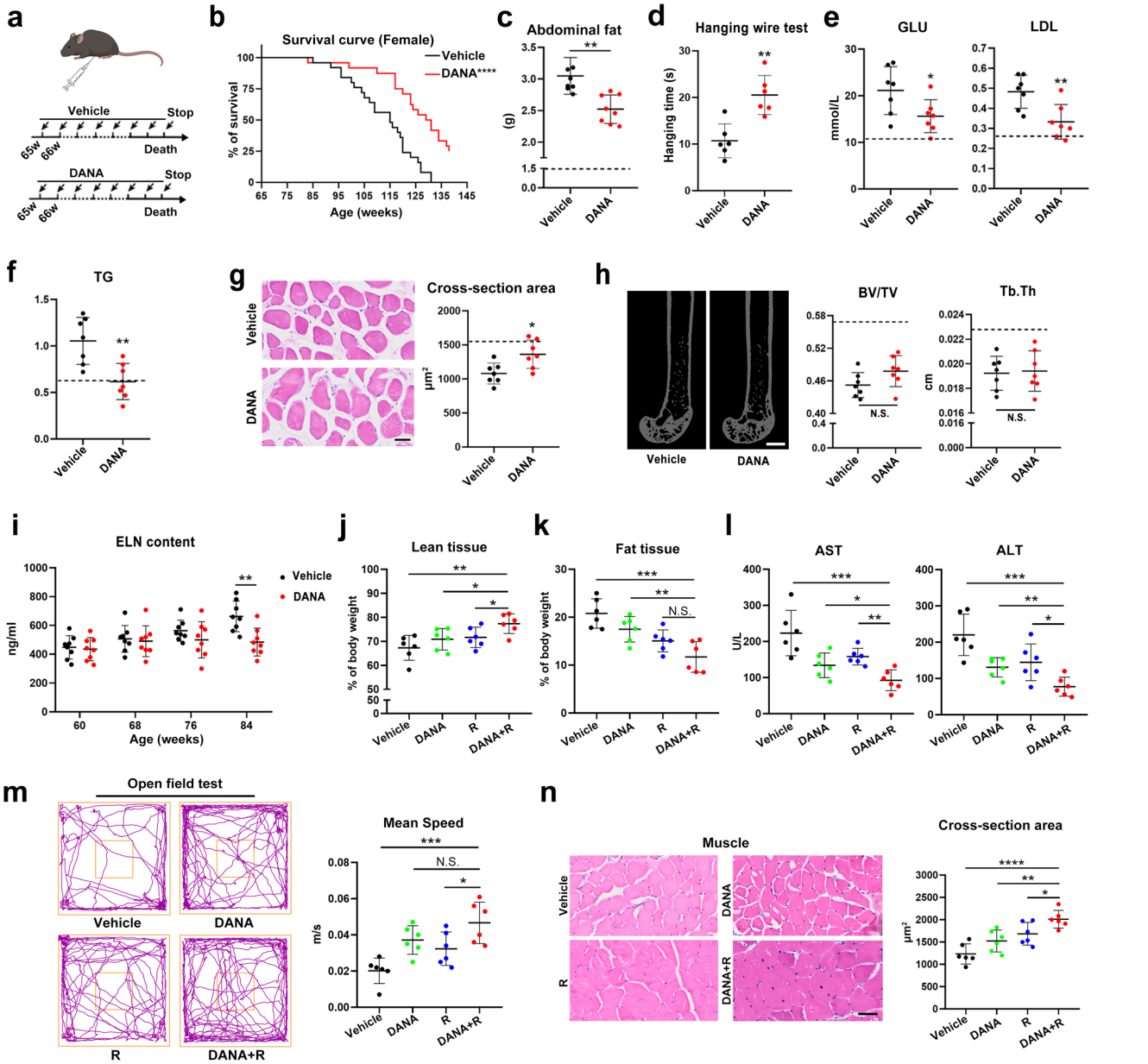

Extended Data Fig. 9 | DANA monotherapy or combined with Rapamycin alleviates aging in naturally-aged mice. a, Illustrative representation of DANA treatment regimen. Illustration was created using FigDraw. **b**, Survival curves for mice treated with DANA or vehicle (vehicle: n = 25, DANA: n = 24; DANA versus vehicle $P < 0.0001$ by log-rank test and $P = 0.0003$ by Gehan–Breslow–Wilcoxon test). **c**, Abdominal fat weight of mice (vehicle: n = 7, DANA: n = 8, DANA versus vehicle $P = 0.0012$) at the experimental endpoint (84 weeks of age). **d**, Statistical hanging time of hang wire test (n = 6 per group, DANA versus vehicle $P = 0.0015$). **e**,**f**, Levels of serum biochemistry markers (TG, LDL, and GLU) in mice (n = 7 per group, GLU: DANA versus vehicle $P = 0.0376$; LDL: DANA versus vehicle $P = 0.0061$; TG: DANA versus vehicle $P = 0.0034$). **g**, Representative H&E-stained images of muscle fiber (left) and the quantification of cross-sectional areas (right) (n = 7 per group, scale bar = 50 μm, DANA versus vehicle $P = 0.0134$). **h**, Representative micro-CT images of bone tissue and the quantification of BV/TV and Tb.Th (n = 7 per group, scale bar = 1 mm). **i**, Serum levels of ELN fragments (n = 8 per group, DANA versus vehicle $P = 0.0035$). $^{*}p < 0.05$, $^{**}p < 0.01$. The black dashed line in bar plots indicates the average value for middle-aged mice (36 weeks of age). **j**,**k**, The proportion of lean tissue (**j**) or fat tissue (**k**) to the total body weight in mice at the experimental endpoint, 84 weeks (n = 6 per group, Lean tissue: DANA + R versus vehicle $P = 0.0040$, DANA + R versus DANA $P = 0.0263$, DANA + R versus R $P = 0.0395$; Fat tissue: DANA + R versus vehicle $P = 0.0005$, DANA + R versus DANA $P = 0.0069$). **l**, Serum levels of AST (left) and ALT (right) (n = 6 per group, AST: DANA + R versus vehicle $P = 0.0009$, DANA + R versus DANA $P = 0.0456$, DANA + R versus R $P = 0.0014$; ALT: DANA + R versus vehicle $P = 0.0002$, DANA + R versus DANA $P = 0.0059$, DANA + R versus R $P = 0.0163$). **m**, Open field test, including movement trajectories (left) and average speed (right) (n = 6 per group, DANA + R versus vehicle $P = 0.0007$, DANA + R versus R $P = 0.0379$). **n**, Representative H&E-stained images of muscle fibers (left) and quantification of cross-sectional areas (right) (n = 6 per group, DANA + R versus vehicle $P < 0.0001$, DANA + R versus DANA $P = 0.0035$, DANA + R versus R $P = 0.0319$). $^{*}P < 0.05$, $^{**}P < 0.01$, $^{***}P < 0.001$, $^{****}P < 0.0001$. Scale bar = 1 mm for **h**, scale bar = 50 μm for **g**,**n**. Unpaired two-tailed Student's t-test with a two-tailed 95% confidence interval (**c**-**h**). Log-rank test and Gehan–Breslow–Wilcoxon test (**b**). Two-way ANOVA (**i**-**n**).

https://doi.org/10.1038/s43587-025-00961-8

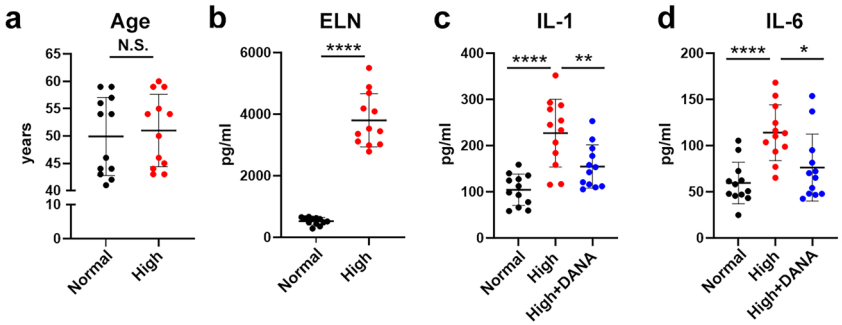

Extended Data Fig. 10 | DANA alleviates the inflammatory response of human macrophages induced by human serum with high content of ELN fragments. **a**, Age statistics of serum samples from high ELN fragments (High) and normal ELN fragments (Normal) population (n = 12 per group). **b**, Statistics of serological ELN contents in each group (n = 12 per group, High versus Normal $p < 0.0001$). **c**,**d**, Inflammatory cytokines including IL-1 and IL-6 in cultural supernatant of macrophages derived from THP-1 cells among Normal, High+DANA and High group (n = 12 per group, IL-1: High versus Normal $P < 0.0001$, High+DANA versus High $P = 0.0086$; IL-6: High versus Normal $P < 0.0001$, High+DANA versus High $P = 0.0109$). * $P < 0.05$, ** $P < 0.01$, **** $P < 0.0001$. Unpaired two-tailed Student's t-test (equal variance) or unpaired two-tailed with Welch's correction (unequal variance) (**a**-**d**).

nature portfolio

Corresponding author(s): Hongwei Ouyang

Last updated by author(s): Jul 15, 2025

Reporting Summary

Nature Portfolio wishes to improve the reproducibility of the work that we publish. This form provides structure for consistency and transparency in reporting. For further information on Nature Portfolio policies, see our Editorial Policies and the Editorial Policy Checklist.

Statistics

For all statistical analyses, confirm that the following items are present in the figure legend, table legend, main text, or Methods section.

n/a	Confirmed
☐	☒ The exact sample size (*n*) for each experimental group/condition, given as a discrete number and unit of measurement
☐	☒ A statement on whether measurements were taken from distinct samples or whether the same sample was measured repeatedly
☐	☒ The statistical test(s) used AND whether they are one- or two-sided *Only common tests should be described solely by name; describe more complex techniques in the Methods section.*
☒	☐ A description of all covariates tested
☐	☒ A description of any assumptions or corrections, such as tests of normality and adjustment for multiple comparisons
☐	☒ A full description of the statistical parameters including central tendency (e.g. means) or other basic estimates (e.g. regression coefficient) AND variation (e.g. standard deviation) or associated estimates of uncertainty (e.g. confidence intervals)
☐	☒ For null hypothesis testing, the test statistic (e.g. *F*, *t*, *r*) with confidence intervals, effect sizes, degrees of freedom and *P* value noted *Give P values as exact values whenever suitable.*
☒	☐ For Bayesian analysis, information on the choice of priors and Markov chain Monte Carlo settings
☐	☒ For hierarchical and complex designs, identification of the appropriate level for tests and full reporting of outcomes
☒	☐ Estimates of effect sizes (e.g. Cohen's *d*, Pearson's *r*), indicating how they were calculated

Our web collection on statistics for biologists contains articles on many of the points above.

Software and code

Policy information about availability of computer code

Data collection	I declare that no software was used.
Data analysis	The software used for data analysis including GraphPad Prism (8.0), Flowjo (10.8.1), xvViewer (3.27.0.27564), and R (4.4.2).

For manuscripts utilizing custom algorithms or software that are central to the research but not yet described in published literature, software must be made available to editors and reviewers. We strongly encourage code deposition in a community repository (e.g. GitHub). See the Nature Portfolio guidelines for submitting code & software for further information.

Data

Policy information about availability of data

All manuscripts must include a data availability statement. This statement should provide the following information, where applicable:

- Accession codes, unique identifiers, or web links for publicly available datasets
- A description of any restrictions on data availability
- For clinical datasets or third party data, please ensure that the statement adheres to our policy

The row data of CyTOF in this paper have been deposited in the OMIX, China National Center for Bioinformation / Beijing Institute of Genomics, Chinese Academy of Sciences (https://ngdc.cncb.ac.cn/omix: accession no. OMIX006334). The raw data of RNA-seq reported in this paper have been deposited in the Genome Sequence Archive (Genomics, Proteomics & Bioinformatics 2021) in National Genomics Data Center (Nucleic Acids Res 2022), China National Center for Bioinformation / Beijing Institute of Genomics, Chinese Academy of Sciences (GSA: CRA016019) that are publicly accessible at https://ngdc.cncb.ac.cn/gsa. The raw data of single-cell

RNA-seq have been deposited in the Genome Sequence Archive at the National Genomics Data Center, China National Center for Bioinformation / Beijing Institute of Genomics, Chinese Academy of Sciences (GSA: CRA025173) and are publicly accessible at https://ngdc.cncb.ac.cn/gsa. All data in this article are provided in source data file or available upon reasonable request from the corresponding authors.

Research involving human participants, their data, or biological material

Policy information about studies with human participants or human data. See also policy information about sex, gender (identity/presentation), and sexual orientation and race, ethnicity and racism.

Reporting on sex and gender	We did not select based on sex and gender in the cohort of 1068 serum samples (male : female = 553 : 515).
Reporting on race, ethnicity, or other socially relevant groupings	We did not select based on race, ethnicity, or other socially relevant groupings.
Population characteristics	We did not select based on population characteristics.
Recruitment	We collected data without any bias in the recruitment process. These people were excluded: (1) people during pregnancy; (2) people suffered from congenital or hereditary anemia, HIV, end-stage kidney disease, cirrhosis, blood cancer, BM transplant and splenectomy, or other severe motor and/or mental disturbance; (3) people that predicted lifespan were lower than 1 years.
Ethics oversight	The detection and analysis of clinical samples in this study were under the ethical approval of the Fourth Affiliated Hospital Zhejiang University School of Medicine (K2022171). Registration and giving informed written consent were performed.

Note that full information on the approval of the study protocol must also be provided in the manuscript.

Field-specific reporting

Please select the one below that is the best fit for your research. If you are not sure, read the appropriate sections before making your selection.

☒ Life sciences ☐ Behavioural & social sciences ☐ Ecological, evolutionary & environmental sciences

For a reference copy of the document with all sections, see nature.com/documents/nr-reporting-summary-flat.pdf

Life sciences study design

All studies must disclose on these points even when the disclosure is negative.

Sample size	No statistical methods were used to pre-determine sample size, but the sample sizes are similar to those in previously published works in the field.
Data exclusions	Outliers were excluded from the analyses.
Replication	All experimental groups contained at least three biological replicates.
Randomization	Allocations were random.
Blinding	Investigators were blinded to group allocation during data collection and analysis.

Reporting for specific materials, systems and methods

We require information from authors about some types of materials, experimental systems and methods used in many studies. Here, indicate whether each material, system or method listed is relevant to your study. If you are not sure if a list item applies to your research, read the appropriate section before selecting a response.

Materials & experimental systems

n/a	Involved in the study
☐	☒ Antibodies
☐	☒ Eukaryotic cell lines
☒	☐ Palaeontology and archaeology
☐	☒ Animals and other organisms
☐	☒ Clinical data
☒	☐ Dual use research of concern
☒	☐ Plants

Methods

n/a	Involved in the study
☒	☐ ChIP-seq
☐	☒ Flow cytometry
☒	☐ MRI-based neuroimaging

Antibodies

Antibodies used

1. CD45-APC, eBioscience, 17-0454-811, 104 (1:50 for Flow Cyt)
2. CD45-FITC, Biolegend, 103107, 30-F11 (1:50 for Flow Cyt)
3. CD11b-FITC, Biolegend, 101205, M1/70 (1:50 for Flow Cyt)
4. CD3e-FITC, Invitrogen, 11-0031-82, 145-2C11 (1:50 for Flow Cyt)
5. CD3e-APC/Cy7, Biolegend, 100221, 17A2 (1:50 for Flow Cyt)
6. CD19-APC/Cy7, Biolegend, 115529, 6D5 (1:50 for Flow Cyt)
7. CD19-PE, Biolegend, 115507, 6D5 (1:50 for Flow Cyt)
8. Ly6G-APC/Cy7, Biolegend, 127623, 1A8 (1:50 for Flow Cyt)
9. Ly6G-APC, Biolegend, 127613, 1A8 (1:50 for Flow Cyt)
10. NK1.1-APC, Biolegend, 156505, S17016D (1:50 forFlow Cyt)
11. NK1.1-APC/Cy7, Biolegend, 108723, PK136 (1:50 forFlow Cyt)
12. CD170-APC/Cy7 (SiglecF), Biolegend, 155531, S17007L (1:50 forFlow Cyt)
13. NEU1, Santa Cruz, sc-166824, F-8 (1:1000 for WB)
14. Tubulin, CST, 2144 (1:3000 for WB)
15. Anti-mouse HRP, Jackson Immuno Research, 115-035-003 (1:5000 for WB)
16. Anti-rabbit HRP, ABclonal, AS014 (1:5000 for WB)
17. IL-1b, R&D Systems, MAB401 (5 mg/kg for Neutralization)
18. IL-6, R&D Systems, MAB406 (2 mg/kg for Neutralization)
19. MIP-1a, R&D Systems, AF-450 (2 mg/kg for Neutralization)
20. Elastin, Sigma, E4013, BA-4 (5 mg/kg for Neutralization)

Validation

All the antibodies in this study are commercially available and have been applied and validated in multiple published research studies.

Eukaryotic cell lines

Policy information about cell lines and Sex and Gender in Research

Cell line source(s)

Bone marrow-derived macrophages were isolated from femurs and tibias from wild-type or LysM-Cre/Neu1-flox male mice. bone marrow was flushed with culture medium using a 1 ml syringe for acquiring bone marrow-derived macrophages. BMDMs were cultured and purified in low-glucose Dulbecco's modified Eagle's medium (L-DMEM, C11885500BT, Gibco, USA) containing 10% FBS and M-CSF (CB34, Novoprotein, China).

Authentication

None of the cell lines used were authenticated.

Mycoplasma contamination

Cell lines tested negative for mycoplasma contamination.

Commonly misidentified lines
(See ICLAC register)

No commonly misidentified lines used.

Animals and other research organisms

Policy information about studies involving animals; ARRIVE guidelines recommended for reporting animal research, and Sex and Gender in Research

Laboratory animals

Wild type C57BL/6J mice (12, 40, 60, 65, 68, 70-week-old); P16-3MR mice (12, 60-week-old); Rag1 gene knockout mice (8, 30-week-old); LysM/iDTR mice (24-week-old); LysM-Cre/Neu1-flox mice (12-week-old); Neu1 gene knockout mice (12-week-old); Yorkshire pigs (24-week-old); NDG-hIL15 mice (24-week-old).

Wild animals

I declare that the study did not involve wild animals.

Reporting on sex

Male animals were primarily used to verify the findings.

Field-collected samples

I declare that the study did not involve samples collected from the field.

Ethics oversight

Animal experiments were conducted with the approval of the Zhejiang University Experimental Animal Welfare and Ethics Committee (ZJU20230096 for mice experiments, ZJU20240053 for pig experiments).

Note that full information on the approval of the study protocol must also be provided in the manuscript.

Clinical data

Policy information about clinical studies

All manuscripts should comply with the ICMJE guidelines for publication of clinical research and a completed CONSORT checklist must be included with all submissions.

Clinical trial registration

No clinical trial.

Study protocol

Note where the full trial protocol can be accessed OR if not available, explain why.

Data collection	*Describe the settings and locales of data collection, noting the time periods of recruitment and data collection.*
Outcomes	*Describe how you pre-defined primary and secondary outcome measures and how you assessed these measures.*

Plants

Seed stocks	*Report on the source of all seed stocks or other plant material used. If applicable, state the seed stock centre and catalogue number. If plant specimens were collected from the field, describe the collection location, date and sampling procedures.*
Novel plant genotypes	*Describe the methods by which all novel plant genotypes were produced. This includes those generated by transgenic approaches, gene editing, chemical/radiation-based mutagenesis and hybridization. For transgenic lines, describe the transformation method, the number of independent lines analyzed and the generation upon which experiments were performed. For gene-edited lines, describe the editor used, the endogenous sequence targeted for editing, the targeting guide RNA sequence (if applicable) and how the editor was applied.*
Authentication	*Describe any authentication procedures for each seed stock used or novel genotype generated. Describe any experiments used to assess the effect of a mutation and, where applicable, how potential secondary effects (e.g. second site T-DNA insertions, mosiacism, off-target gene editing) were examined.*

Flow Cytometry

Plots

Confirm that:

☒ The axis labels state the marker and fluorochrome used (e.g. CD4-FITC).

☒ The axis scales are clearly visible. Include numbers along axes only for bottom left plot of group (a 'group' is an analysis of identical markers).

☒ All plots are contour plots with outliers or pseudocolor plots.

☒ A numerical value for number of cells or percentage (with statistics) is provided.

Methodology

Sample preparation	Sample was collected from mouse peripheral blood or spleen. Blood or spleen samples were collected and red blood cells were lysed. Cells were resuspended and stained with antibodies for 60 min on ice in dark. Wash cells with PBS and resuspend in PBS for flow cytometry analysis.
Instrument	The flow cytometry analyzer (Cytoflex, Beckman, USA) was used.
Software	Data was analyzed with the Flowjo software (v10.8.1).
Cell population abundance	Cells were stained as follows: B cell (CD45+, CD19+), T cell (CD45+, CD3E+), neutrophil (CD45+, CD11B+, LY6G+), monocyte/macrophage (CD45+, CD11B+, LY6G-, CD3E-, CD19-, NK1.1-, SiglecF-).
Gating strategy	Live cells were gated with FSC/SSA, and doublets were excluded based on FSC-H/FSC-A. Immune cells were stained as CD45+ and subset cells were further defined based on multiple markers as follows: B cell (CD45+, CD19+), T cell (CD45+, CD3E+), neutrophil (CD45+, CD11B+, LY6G+), monocyte/macrophage (CD45+, CD11B+, LY6G-, CD3E-, CD19-, NK1.1-, SiglecF-).

☒ Tick this box to confirm that a figure exemplifying the gating strategy is provided in the Supplementary Information.